A Stable and Accurate Partitioned Algorithm for Conjugate Heat Transfer

F. Meng[a,1], J. W. Banks[b,1,3,*], W. D. Henshaw[b,1,2], D. W. Schwendeman[b,1,2]

[a] *Department of Mechanical, Aerospace and Nuclear Engineering, Rensselaer Polytechnic Institute, Troy, NY 12180, USA*

[b] *Department of Mathematical Sciences, Rensselaer Polytechnic Institute, Troy, NY 12180, USA*

Abstract

We describe a new partitioned approach for solving conjugate heat transfer (CHT) problems where the governing temperature equations in different material domains are time-stepped in a implicit manner, but where the interface coupling is explicit. The new approach, called the CHAMP scheme (Conjugate Heat transfer Advanced Multi-domain Partitioned), is based on a discretization of the interface coupling conditions using a generalized Robin (mixed) condition. The weights in the Robin condition are determined from the optimization of a condition derived from a local stability analysis of the coupling scheme. The interface treatment combines ideas from optimized-Schwarz methods for domain-decomposition problems together with the interface jump conditions and additional compatibility jump conditions derived from the governing equations. For many problems (i.e. for a wide range of material properties, grid-spacings and time-steps) the CHAMP algorithm is stable and second-order accurate using no sub-time-step iterations (i.e. a single implicit solve of the temperature equation in each domain). In extreme cases (e.g. very fine grids with very large time-steps) it may be necessary to perform one or more sub-iterations. Each sub-iteration generally increases the range of stability substantially and thus one sub-iteration is likely sufficient for the vast majority of practical problems.

The CHAMP algorithm is developed first for a model problem and analyzed using normal-mode theory. The theory provides a mechanism for choosing *optimal* parameters in the mixed interface condition. A comparison is made to the classical Dirichlet-Neumann (DN) method and, where applicable, to the optimized-Schwarz (OS) domain-decomposition method. For problems with different thermal conductivities and diffusivities, the CHAMP algorithm outperforms the DN scheme. For domain-decomposition problems with uniform conductivities and diffusivities, the CHAMP algorithm performs better than the typical OS scheme with one grid-cell overlap. The CHAMP scheme is also developed for general curvilinear grids and CHT examples are presented using composite overset grids that confirm the theory and demonstrate the effectiveness of the approach.

Keywords: conjugate heat transfer, optimized Schwarz method, domain decomposition, Dirichlet Neumann method, overset grids.

1. Introduction

Conjugate heat transfer (CHT) concerns the coupled heat transfer between fluids and solids, and it plays an important role in many scientific and engineering applications, including modeling heat exchangers or nuclear reactor cores, cooling of micro-channels in electronic packaging, thermal effects in turbo machinery, and more. Depending on the application, there can be any number of different fluid and/or solid domains,

*Department of Mathematical Sciences, Rensselaer Polytechnic Institute, 110 8th Street, Troy, NY 12180, USA.

Email addresses: meng5@rpi.edu (F. Meng), banksj3@rpi.edu (J. W. Banks), henshw@rpi.edu (W. D. Henshaw), schwed@rpi.edu (D. W. Schwendeman)

[1] This work was performed under DOE contracts from the ASCR Applied Math Program.

[2] Research supported by the National Science Foundation under grant DMS-1519934.

[3] Research supported by a U.S. Presidential Early Career Award for Scientists and Engineers.

and the interfaces can be of fluid-fluid, fluid-solid, or solid-solid type. Thermal coupling generally imposes continuity of temperature and heat flux along the interfaces, and this often plays an important role in the overall dynamics of the system. From the perspective of numerical solvers, the discretization of the thermal coupling conditions has a major impact on the overall performance of the solution approach, and this is one of the significant challenges to be addressed in any approach to solving CHT problems.

The main objective of the current study is the design and analysis of partitioned[4] approaches to solving CHT problems where, in particular, we consider partitioned schemes in which the temperature in each subdomain is advanced with an implicit time-stepping method. In contrast to a monolithic approach where a single numerical solver is developed to solve all domains at once, a partitioned approach uses different numerical solvers in the different fluid and solid domains, and these solvers are coupled only at the interface between domains. There are many practical benefits of partitioned methods, including the ability to use specialized or highly optimized domain solvers and the ability to take advantage of disparate time scales in different domains. Also, monolithic methods require the solution of a large system of equations at each time step corresponding to the fully coupled system. Solving this large system can be challenging and costly, and may require the development of specialized preconditioners that account for the eigenstructure of the fully coupled problem. Partitioned methods, on the other hand, do not require the solution of this large coupled system. However, ensuring both the stability and accuracy of partitioned methods for a wide range of material parameters can be a significant challenge. Since the primary difficulty in partitioned approaches for CHT problems concerns the coupling of the temperature in the different domains, in this work we consider a simplified CHT problem where the governing equation in each domain is a heat equation for the temperature alone. Furthermore, since heat equations are generally stiff, an implicit time-stepping scheme is used to advance the temperature in each domain.

The traditional interface treatment for partitioned CHT is known as the Dirichlet-Neumann (DN) coupling in which the temperature of the solid is used as a Dirichlet boundary condition on the fluid while the fluid heat-flux is used as a Neumann boundary condition on the solid. In some regimes the opposite Neumann-Dirichlet (ND) scheme is appropriate to use while in general Robin (mixed) conditions that weight the Dirichlet and Neumann operators with appropriate coefficients may be useful. The development and analysis of methods that make use of these different interface couplings has been the subject of much prior work in the literature. Giles [1], for example, analyzed a discretization of a fluid-solid CHT problem using the classical DN coupling and derived conditions on the material parameters such that the DN coupling would be stable. For the case of explicit time-stepping, Roe *et al.* [2] considered an alternate discrete approximation to the temperature continuity equation which included a compatibility condition. This approached reduced the time-stepping stability constraint to be the smaller of the stable time steps for the solver in each subdomain in isolation. Henshaw and Chand [3] also considered explicit time-stepping schemes, and they developed discrete interface conditions that are stable and second-order accurate for any values of the thermal properties. For the case of implicit time-stepping, Henshaw and Chand analyzed the convergence behavior of sub-time-step iterations for a two-dimensional problem. They found that either the DN coupling or ND coupling converges rapidly when the thermal conductivities and diffusivities of adjacent domains are vastly different, but that the iteration converges slowly when the thermal properties of the materials are nearly identical. The analysis in [3] showed that coefficients can always be chosen for Robin interface conditions so that the sub-time-step iterations converges, and they suggested how to choose these coefficients. Roux and Garaud [4] studied DN, Robin-Dirichlet and Robin-Robin conditions based on a matrix analysis. They showed that the optimal coefficient in the Robin condition could be chosen based on the the Dirichlet-to-Neumann mapping from the coupling domain; however, this mapping is non-local and expensive to compute. Heselhaus [5] used mode analysis to study stability of a conjugate heat transfer problem for a turbine blade calculation where the time-dependent fluid equations were coupled to steady-state equations for the solid. Two different coupling schemes were analyzed and it was shown that a coupling based on heat flux is unconditionally unstable while a coupling based on a virtual ambient temperature is stable within certain stability constraints on the time step. Errera and Chemin [6] considered a CHT problem with a one-dimensional unsteady fluid coupled to a quasi steady-state solid and determined optimal weightings for which Robin interface conditions remain stable within a time-stepping scheme.

[4]Partitioned schemes are sometimes called segregated or weakly-coupled schemes.

When there is no jump in material properties across the interface, the CHT problem reduces to a domain decomposition (DD) problem, for which there is a large body of published work. Of particular interest is the development of the Schwarz iteration [7] that uses mixed or Robin-type coupling conditions in order to accelerate the convergence of the iteration. Recently there have been significant developments in the determination of optimal coefficients for Robin-type interface conditions for DD. In [8], for example, Gander developed an approach to determine optimal weights for a Robin condition in Schwarz domain-decomposition. After Fourier-transforming in the tangential directions to the interface, the exact solution to a model problem is used to determine optimal weights for the Robin conditions in this transformed space. However, upon applying the inverse transform, a global operator in physical space is implied. In order to obtain a local condition, the optimal weights in the transformed space are approximated, eventually leading to local Robin and generalized Robin operators in physical space; the so-called "optimized Schwarz" method. Following these developments, Gander and Dubois [9] extended Schwarz-like iterations to steady state CHT problems with disparate materials. They introduced new mixed interface conditions with weightings determined to optimize the convergence rate of the iteration for small mesh size, or similarly large jumps in the thermal conductivities. One important aspect affecting the performance of Schwarz-type iterations is the use of domain overlap. In particular, it has been known for decades that the inclusion of domain overlap yields exponentially faster iteration convergence rates for increasing wave number in the transverse direction. For the DD problem, including domain overlap is a straightforward proposition, and the resulting schemes have ben extensively studied. However, for the CHT problem, increasing the domain overlap is less obvious, and indeed in [9] only the non-overlapping Schwarz iteration is investigated. It is the purpose of the current article to show one approach for incorporating domain overlap into the CHT problem.

For the case of time-dependent CHT problems where partitioned time-stepping is employed, an iteration is generally performed at each time step. If this iteration is not executed to convergence, an accurate initial guess, typically obtained through time extrapolation, is required at each time step in order to maintain the desired order of accuracy. This issue was addressed in Peet and Fischer [10] who studied domain decomposition for the heat equation. They analyzed the stability and accuracy of the time-stepping scheme, which used implicit time-stepping for each domain and various choices of time extrapolation to initiate the coupling iteration. They proved that their un-iterated time-stepping scheme is unconditionally stable for any domain overlap size using first-order accurate interface extrapolation and first or second-order backward-difference-formula time-stepping schemes; however, the resulting schemes remain only first-order accurate. With higher-order accurate interface extrapolations or higher-order time integration methods, however, their schemes may require increasing the number of sub-time-step iterations.

In the current work, we extend the existing work on Schwarz-like iterations to derive a generalized Robin interface condition for partitioned CHT schemes that includes the beneficial effects of domain overlap. The Dirichlet-like and Neumann-like components of the Robin condition are derived following ideas from Henshaw and Chand [3], while their relative weighting is obtained following the discussion in Gander [8]. The scheme can therefore be viewed as a hybrid of recent Robin coupling type conditions for FSI problems [11–17] together with overlapping optimized Schwarz domain decomposition [8] extended to the case of disparate thermal conductivities and diffusivities. This new scheme is called the **C**onjugate **H**eat transfer **A**dvanced **M**ulti-domain **P**artitioned method, or CHAMP method for short. A key ingredient in the derivation of the CHAMP method is the use of a Taylor expansion in space at a distance h from the interface along with the interface conditions and governing equations to relate the solution and its derivatives on one side of the interface to those on the other side. The resulting generalized Robin conditions contain higher-order derivative information than traditional Robin conditions, and they embed an overlap of width h into the conditions which improves the convergence rate of the iteration, particularly for high wave numbers in the transverse direction to the boundary.

The CHAMP coupling conditions are analyzed first as fixed-point iteration (i.e. iterating at a fixed time) and the convergence rate is found to be better than the traditional DN scheme for any choice of the material parameters. For the special case when the properties are equal across a material interface (i.e. traditional domain decomposition) the convergence rate is also found to be better than a typical form of the optimized-Schwarz domain-decomposition method of Gander [8]. The corresponding CHAMP time-stepping algorithm is analyzed next. This scheme employs an accurate initial guess for the CHAMP interface conditions and uses a fixed number of iterations, without regard to any convergence criteria. With no iterations, the CHAMP time-stepping scheme requires only one implicit PDE solve in each domain, and

this un-iterated scheme is found to be stable for spatial and temporal grid spacings which encompass a wide range of practically realizable simulations. Additional iterations may be required to ensure stability for more difficult problems with large time-steps and finer mesh spacings where the beneficial effect of the overlap, h, is reduced. However, the dimensionless parameters of the problem indicate that a single iteration of the CHAMP interface conditions (requiring two PDE solves in each domain) would be sufficient for the vast majority of two- and three-dimensional simulations of practical interest. Example problems in two dimensions are used to evaluate the CHAMP method. To treat complex geometry, each solid domain is discretized using a composite overlapping grid [18], also known as an overset or Chimera grid. This provides an efficient means to generate a composite structured grid, with boundary conforming grids, for complex and possibly moving geometries. The current paper restricts its attention to coupled heat transfer problems in two dimensions. Extensions to problems in three dimensions and to CHT problems involving incompressible and compressible fluid flow will be considered in future work.

An outline of the remainder of this paper is as follows. Section 2 defines the governing equations for the coupled heat transfer problems under consideration. Section 3 then introduces a simple model problem that will be used to discuss the performance of the traditional Dirichlet-Neumann scheme in Section 3.1 and the overlapping optimized Schwarz method for domain decomposition in Section 3.2. The new CHAMP method is developed in Section 3.3, and an analysis of the convergence rate when iterating is presented in that same section. Extension and analysis of the CHAMP method to the case of time-stepping is presented in Section 4. To treat complex geometrical situations, Section 5 presents the CHAMP method on curvilinear grids in the context of composite overset grids. Results from numerical experiments are given in Section 6, and some concluding remarks are given in Section 7. In Appendix A the accuracy of the un-iterated CHAMP scheme is studied and the scheme is shown to be second-order accurate for a one-dimensional CHT problem.

2. Problem specification and governing equations

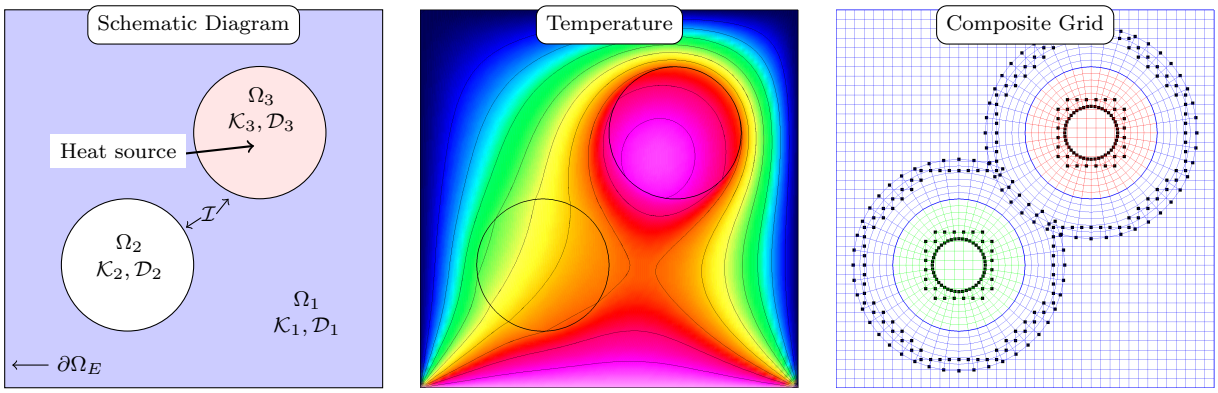

Figure 1: An example of a conjugate heat transfer problem with three different sub-domains, one square with material properties $(\mathcal{K}_1, \mathcal{D}_1)$ and two disks with material properties $(\mathcal{K}_2, \mathcal{D}_2)$ and $(\mathcal{K}_3, \mathcal{D}_3)$ respectively. The boundary at the bottom of the square region is heated and a heat source is added in disk Ω_3. At left is a schematic representation of this problem, in middle is the computed temperature at one time, and at right is a coarse version of the composite grid used for the calculations in Section 6.3.2.

Consider the simplified CHT problem of coupled heat transfer in different materials, an example of which is depicted in Figure 1. The global domain, denoted by Ω, is the union of a set of M non-overlapping subdomains Ω_m, $m = 1, 2, \ldots, M$, that represent distinct regions of different material properties. The interface between different subdomains is denoted $\mathcal{I}$, and the exterior boundary of the domain is given by $\partial\Omega_E$. By convention, the unit normal $\mathbf{n}$ is chosen to point outward from the domain with higher index m, and outward at exterior boundaries. Let $\left[f\right]_{\mathcal{I}}$ denote the jump in f across the interface $\mathcal{I}$. In this setting,

the equations governing the temperature are given as (see, for example, Carslaw [19])

$$\partial_t T = \frac{1}{\rho C}\nabla\cdot(\mathcal{K}\nabla T) + f(\mathbf{x},t), \qquad \mathbf{x}\in\Omega, \tag{1}$$

$$a\,T + b\,\mathbf{n}\cdot\nabla T = g(\mathbf{x},t), \qquad \mathbf{x}\in\partial\Omega_E, \quad \text{(exterior BCs)} \tag{2}$$

$$\big[T\big]_{\mathcal{I}} = 0, \qquad \mathbf{x}\in\mathcal{I}, \quad \text{(interface temperature continuity)} \tag{3}$$

$$\big[\mathcal{K}\mathbf{n}\cdot\nabla T\big]_{\mathcal{I}} = 0, \qquad \mathbf{x}\in\mathcal{I}, \quad \text{(interface heat flux continuity)} \tag{4}$$

$$T(\mathbf{x},0) = T^{\text{IC}}(\mathbf{x}), \qquad \mathbf{x}\in\Omega \quad \text{(initial conditions)} \tag{5}$$

where $T = T(\mathbf{x},t)$ is the temperature, $\mathcal{K} = \mathcal{K}(\mathbf{x})$ the thermal conductivity, $\rho = \rho(\mathbf{x})$ the density, $C = C(\mathbf{x})$ the specific heat, and $f = f(\mathbf{x},t)$ is a heat source. Equation (2) denotes some appropriate mixed, Neumann or Dirichlet boundary condition (BC) on the exterior of the domain with coefficients $a(\mathbf{x},t)$, $b(\mathbf{x},t)$ and forcing $g(\mathbf{x},t)$. For simplicity we assume that $\mathcal{K}$, ρ and C are constant over each subdomain Ω_m. Note that we have used the notation ∂_t to denote the partial derivative with respect to time, with spatial derivatives similarly defined.

3. Model equations and analysis

As discussed in the introduction, the focus in this manuscript is the development and analysis of partitioned solvers for CHT problems such as the one given in (1)–(5). To more clearly introduce and analyze different approaches to interface coupling, we consider a simplified two-material model problem as shown in Figure 2 consisting of planar interface, $\mathcal{I} = 0\times[0,2\pi)$, separating two materials without external forcing. The domain to the left is $\Omega_L = (-\infty,0)\times[0,2\pi)$, and to the right is $\Omega_R = [0,\infty)\times[0,2\pi)$. For this configuration the system to be analyzed is

$$\partial_t T_m = \mathcal{D}_m \Delta T_m, \qquad \text{for } \mathbf{x}\in\Omega_m, \tag{6}$$

$$\big[T(0,y)\big]_{\mathcal{I}} = 0, \qquad \text{for } y\in(0,2\pi), \tag{7}$$

$$\big[\mathcal{K}\partial_x T(0,y)\big]_{\mathcal{I}} = 0, \qquad \text{for } y\in(0,2\pi), \tag{8}$$

$$T_m(x,y+2\pi,t) = T_m(x,y,t), \qquad \text{for } \mathbf{x}\in\Omega_m, \tag{9}$$

$$\|T_m\|_2 < \infty, \tag{10}$$

$$T_m(\mathbf{x},0) = T_m^{\text{IC}}(\mathbf{x}), \qquad \text{for } \mathbf{x}\in\Omega_m, \tag{11}$$

where $m = L, R$ indicates the left or right domain, and $\mathcal{D}_m = \mathcal{K}_m/(\rho_m C_m)$ is the constant thermal diffusivity in each domain. The initial conditions, $T_m^{\text{IC}}(\mathbf{x})$, are assumed to be of compact support and we look for solutions that are periodic in y and of bounded L_2-norm which implies $T\to 0$ as $|x|\to\infty$.

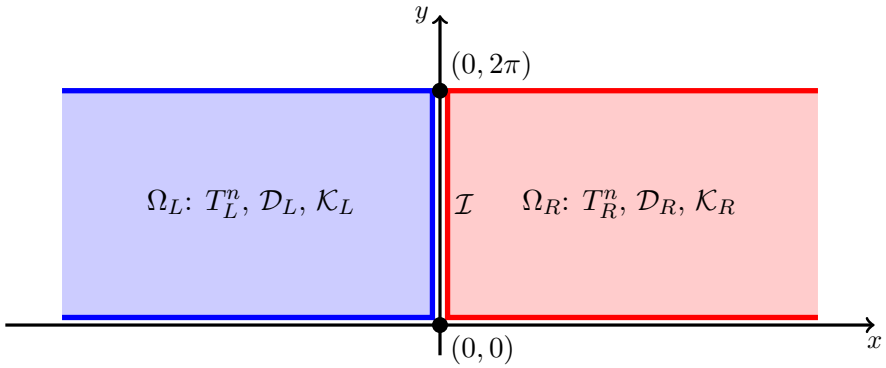

Figure 2: The geometry for the model problems. The solution is assumed to be 2π-periodic in the y-direction.

The equations (6)–(11) are discretized with a method-of-lines approach, discretizing in time, while keeping space continuous (which clarifies the presentation). The second-order accurate backward-difference for-

mula (BDF2) is used to advance the solution in time, and this gives

$$T_m^{n+1} - \frac{4}{3}T_m^n + \frac{1}{3}T_m^{n-1} = \frac{2\Delta t}{3}\left(\mathcal{D}_m \Delta T_m^{n+1}\right), \qquad \text{for } \mathbf{x} \in \Omega_m, \tag{12}$$

$$\left[T^{n+1}(0,y)\right]_{\mathcal{I}} = 0, \qquad \text{for } y \in (0,2\pi), \tag{13}$$

$$\left[\mathcal{K}\partial_x T^{n+1}(0,y)\right]_{\mathcal{I}} = 0, \qquad \text{for } y \in (0,2\pi), \tag{14}$$

$$T_L^{n+1}(-\infty,y) = 0, \quad T_R^{n+1}(\infty,y) = 0, \qquad \text{for } y \in (0,2\pi), \tag{15}$$

where superscripts are used to indicate the time level as in $T_m^n \approx T_m(\mathbf{x},t^n)$ with $t^n = n\Delta t$. Note that BDF2 was chosen because it has the stability property of stiff decay, but there are obviously other possible choices for implicit time-stepping. Section 4 discusses why BDF2 was chosen by comparing with Crank-Nicolson (implicit trapezoidal rule in time). Also note that as with all multistep methods, multiple past time levels are required to execute a time step. At the initial time, these past time values can be evaluated using the known solution (e.g. for manufactured solutions) or with a single-step method. The system in (12)–(15) is monolithic and after discretizing in space would require the solution to a large globally coupled linear system.

In a partitioned approach, approximate solutions to (12)–(15) are found by successively solving the implicit equations on each domain separately using some appropriate interface condition, together with a provisional choice for the solution on other domains. In a strongly-coupled partitioned approach this iteration is repeated until the interface conditions are satisfied to a specified tolerance. In a weakly-coupled approach, only a small fixed number of iterations are performed. The particular choice of discrete interface conditions used to couple the sub-domains can have significant impact on the performance of the scheme (accuracy and stability) and this is the subject of the analysis to follow. We will be concerned with both the convergence of the iteration in isolation, and also the convergence of the time-stepping scheme when a fixed number of iterations, even including the case of zero iterations, are taken per time-step.

Letting $T_m^{(j)}$, $j = 0,1,2\ldots$ denote a sequence of iterates which approximate T_m^{n+1}, and letting

$$F_m(\mathbf{x}) = \frac{2}{\mathcal{D}_m \Delta t}T_m^n - \frac{1}{2\mathcal{D}_m\Delta t}T_m^{n-1},$$

then each stage of the iteration requires the solution to two Helmholtz boundary values problems,

$$\frac{1}{\frac{2}{3}\mathcal{D}_m\Delta t}T_m^{(j)} - \Delta T_m^{(j)} = F_m(\mathbf{x}), \qquad \text{for } \mathbf{x} \in \Omega_m, \quad m = L,R, \tag{16}$$

$$\mathcal{B}_L(T_L^{(j)}) = \mathcal{B}_{LR}(T_R^{(j-1)}), \quad \text{or} \quad \mathcal{B}_R(T_R^{(j)}) = \mathcal{B}_{RL}(T_L^{(j)}), \qquad \text{for } \mathbf{x} \in \mathcal{I}, \tag{17}$$

$$T_m^{(j)} \to 0, \qquad \text{for } |x| \to \infty. \tag{18}$$

The operators $\mathcal{B}_L$, $\mathcal{B}_{LR}$, $\mathcal{B}_R$ and $\mathcal{B}_{RL}$ denote the partitioned interface conditions that are used with each sub-domain solve. (These are often a linear combination of the original interface conditions (13)–(14).)

Three important non-dimensional parameters arise in the subsequent analysis; θ, the ratio of the thermal-conductivities, β, the ratio of the thermal-diffusivities, and λ_d, the diffusive time-step parameter,

$$\theta \stackrel{\text{def}}{=} \frac{\mathcal{K}_L}{\mathcal{K}_R}, \quad \beta \stackrel{\text{def}}{=} \frac{\mathcal{D}_L}{\mathcal{D}_R}, \quad \lambda_d \stackrel{\text{def}}{=} \frac{\Delta t \mathcal{D}_L}{h^2}. \tag{19}$$

Here h will either denote the overlap width for an overlapping domain-decomposition method, or h will be proportional to the spatial mesh size; for clarity h is taken to be the same in both domains. In practice, the parameters θ and β can take on a wide range of positive values, with $\theta \approx 1$ often being the difficult case for partitioned solvers. In typical computations λ_d will be large (treating the heat equations as stiff in time).

We will analyze three different discrete interface conditions defining $\mathcal{B}_L$, $\mathcal{B}_{LR}$, $\mathcal{B}_R$ and $\mathcal{B}_{RL}$. The DN interface conditions, given first, are the usual Dirichlet-Neumann interface conditions, with the left domain specifying the heat flux in (20) and the right domain specifying the temperature in (21). Colors are used in the presentation to indicate the *Neumann*-like and *Dirichlet*-like portions of the interface conditions, respectively.

DN Interface Conditions. *Dirichlet-Neumann coupling for CHT*

$$\mathcal{K}_L \partial_x T_L^{(j)}(0,y) = \mathcal{K}_R \partial_x T_R^{(j-1)}(0,y), \tag{20}$$

$$T_R^{(j)}(0,y) = T_L^{(j)}(0,y). \tag{21}$$

The OS interface conditions, given next, represent the overlapping optimized Schwarz scheme of [8], which is applicable for positive overlap $h > 0$ when there is no jump in material properties, i.e. for the case of domain decomposition (DD). Here a linear combination of the Neumann and Dirichlet conditions in (13) and (14) is taken with relative weightings $\mathbf{S}_L$ and $\mathbf{S}_R$. Importantly, this approach incorporates an overlap width h which, when $h > 0$, significantly improves the convergence rate. However, when $h > 0$ the specified approach is apparently not applicable to cases with a jump in material parameters.

OS Interface Conditions. *Overlapping optimized Schwarz coupling for DD (applicable for $h > 0$ when $\mathcal{D}_L = \mathcal{D}_R$ and $\mathcal{K}_L = \mathcal{K}_R$)*

$$\partial_x T_L^{(j)}(h,y) + \mathbf{S}_L T_L^{(j)}(h,y) = \partial_x T_R^{(j-1)}(h,y) + \mathbf{S}_L T_R^{(j-1)}(h,y), \tag{22}$$

$$\partial_x T_R^{(j)}(0,y) - \mathbf{S}_R T_R^{(j)}(0,y) = \partial_x T_L^{(j)}(0,y) - \mathbf{S}_R T_L^{(j)}(0,y). \tag{23}$$

Here h indicates the size of the domain overlap (typically related to the grid spacing), and $\mathbf{S}_L$ and $\mathbf{S}_R$ are linear operators to be specified.

The CHAMP interface conditions, given last, represent the approximations used in the CHAMP method. A detailed description of their derivation is presented in Section 3.3. However, at a high level one can think of these as generalized mixed conditions consisting of a *Neumann* portion and a *Dirichlet* portion, which are combined using the linear operators $\mathbf{S}_L$ and $\mathbf{S}_R$. Both conditions (24) and (25) are applied at the interface $x = 0$, and an effective grid overlap is achieved because the right-hand sides are evaluated at $x = \pm h$.

CHAMP Interface Conditions. *CHAMP coupling for CHT*

$$\Big[\theta\partial_x + h\,\mathcal{L}_\beta\Big] T_L^{(j)}(0,y) \;+\; \mathbf{S}_L\Big[I + \theta h\partial_x + \frac{h^2}{2}\,\mathcal{L}_\beta\Big] T_L^{(j)}(0,y) = \Big[\partial_x + \mathbf{S}_L\Big] T_R^{(j-1)}(h,y), \tag{24}$$

$$\Big[\frac{1}{\theta}\partial_x - h\,\mathcal{L}_{\frac{1}{\beta}}\Big] T_R^{(j)}(0,y) \;-\; \mathbf{S}_R\Big[I - \frac{1}{\theta} h\partial_x + \frac{h^2}{2}\,\mathcal{L}_{\frac{1}{\beta}}\Big] T_R^{(j)}(0,y) = \Big[\partial_x - \mathbf{S}_R\Big] T_L^{(j)}(-h,y), \tag{25}$$

where

$$\mathcal{L}_\gamma \;\stackrel{\text{def}}{=}\; \gamma\,\partial_{xx} + (\gamma - 1)\,\partial_{yy}. \tag{26}$$

Here, h is a domain overlap size (typically the grid spacing), and $\mathbf{S}_L$ and $\mathbf{S}_R$ are linear operators to be specified.

For all three interface conditions, the iteration is updated in a Gauss-Seidel-like procedure with $T_L^{(j)}$ solved first as a function of $T_R^{(j-1)}$, and the result of that computation then used to define $T_R^{(j)}$[5]. All three iteration schemes require a starting guess for $T_R^{(0)}$. The choice of starting guess is important, both to reduce the number of iterations, but also to ensure second-order order accuracy when only a fixed number of iterations are used; this is addressed in Section 4. Furthermore note that since all three schemes use a small local stencil in applying the interface conditions, the cost to perform a single iteration is roughly the same for the three approaches and is dominated by the solution to the heat equations in the domain interior. The partitioned time-stepping scheme for the model problem (with any of the three interface conditions) is represented by the pseudo-code in Algorithm 1.

We note that the analyses of the various interface conditions are performed at the space-continuous level with an overlap of h. The value for h can be any positive value but it is natural to take h to be the grid spacing in the direction normal to the interface; this is what is done in the numerical computations presented later.

[5]Note that although we use a Gauss-Seidel-like procedure in this work, this is by no means required. In particular, one might consider an "additive" procedure with potential advantages for parallel implementation. See also [20] regarding parallel Schwarz methods.

Algorithm 1 Partitioned conjugate heat transfer solver.

Heat-equation solver(Ω, t_{final})
$t = 0$, $n = 0$;
$T_m^0(x,0) = T_m^{\rm IC}(\mathbf{x})$, $m = L, R$; ▷ Initial conditions
while $t < t_{final}$ **do**
  $F_m(\mathbf{x}) = \frac{2}{\mathcal{D}_m \Delta t} T_m^n - \frac{1}{2\mathcal{D}_m \Delta t} T_m^{n-1}$, $m = L, R$; ▷ Assign RHS
  $T_R^{(0)} = \text{Extrapolate}(T_R^n, T_R^{n-1}, \ldots)$; ▷ Initial guess
  for $j = 1, \cdots, N_{\rm si}$ **do** ▷ Sub-time-step iterations
    Solve for $T_L^{(j)}$ *given* $T_R^{(j-1)}$*:*
      $\frac{1}{\frac{2}{3}\mathcal{D}_l \Delta t} T_L^{(j)} - \Delta T_L^{(j)} = F_L$, for $\mathbf{x} \in \Omega_L$;
      $\mathcal{B}_L(T_L^{(j)}) = \mathcal{B}_{LR}(T_R^{(j-1)})$, for $\mathbf{x} \in \mathcal{I}$; ▷ Use (20), (22), or (24)
      $T_L^{(j)}(\mathbf{x}) \to 0$, for $x \to -\infty$;
    Solve for $T_R^{(j)}$ *given* $T_L^{(j)}$*:*
      $\frac{1}{\frac{2}{3}\mathcal{D}_R \Delta t} T_R^{(j)} - \Delta T_R^{(j)} = F_R$, for $\mathbf{x} \in \Omega_R$;
      $\mathcal{B}_R(T_R^{(j)}) = \mathcal{B}_{RL}(T_L^{(j)})$, for $\mathbf{x} \in \mathcal{I}$; ▷ Use (21), (23), or (25)
      $T_R^{(j)}(\mathbf{x}) \to 0$ for $x \to +\infty$;
    error $= \max_{\mathcal{I}} \left\{ \left| \left[T_m^{(j)} \right]_{\mathcal{I}} \right|, \left| \left[\mathcal{K} \partial_n T_m^{(j)} \right]_{\mathcal{I}} \right| \right\}$; ▷ Error in iteration
    If *error* $<$ tol **then** break;
  end for
  $T_m^{n+1} = T_m^{(j)}$, $m = L, R$; ▷ Solution at new time
  $t = t + \Delta t$, $n = n + 1$;
end while

3.1. Analysis of the Dirichlet-Neumann iteration

We begin with a brief derivation the well-known properties of the DN iteration that consists of the inner "**for** j" loop of Algorithm 1 together with the interface conditions (20)–(21). The equations to be solved in each domain define a linear constant-coefficient initial-boundary-value problem, discrete in the time-like iteration count j and continuous in space. The general solution is the sum of a homogeneous solution and a particular solution. The convergence characteristics of the iteration, however, only depend on the solution to the homogeneous problem, which we now analyze. Representing the solution using a Fourier series in y yields

$$T_m(x,y) = \sum_{k=-\infty}^{\infty} \widehat{T}_m(x,k) e^{-iky}, \tag{27}$$

where k is the wave number in the y-direction (i.e. along the interface). The super-imposed *hat* symbol is used throughout the paper to denote the Fourier representation of a variable. Substitution of (27) into the homogeneous equations leads to equations for each Fourier coefficient,

$$(\eta_m + k^2 - \partial_{xx})\, \widehat{T}_m^{(j)} = 0, \tag{28}$$

$$\mathcal{K}_L\, \partial_x \widehat{T}_L^{(j)}(0,k) = \mathcal{K}_R\, \partial_x \widehat{T}_R^{(j-1)}(0,k), \tag{29}$$

$$\widehat{T}_R^{(j)}(0,k) = \widehat{T}_L^{(j)}(0,k), \tag{30}$$

$$\widehat{T}_L^{(j)}(-\infty,k) = 0, \quad \widehat{T}_R^{(j)}(\infty,k) = 0, \tag{31}$$

where

$$\eta_m = \frac{1}{\frac{2}{3}\mathcal{D}_m \Delta t}.$$

The solution of (28) subject to the far-field conditions (31) can be expressed as

$$\widehat{T}_L^{(j)}(x,k) = C_j e^{\sqrt{\eta_L + k^2}\, x}, \tag{32}$$

$$\widehat{T}_R^{(j)}(x,k) = B_j e^{-\sqrt{\eta_R + k^2}\, x}, \tag{33}$$

where C_j and B_j are constants. Substituting (32) and (33) into the interface conditions (29) and (30) gives

$$C_j \mathcal{K}_L \sqrt{\eta_L + k^2} = -B_{j-1} \mathcal{K}_R \sqrt{\eta_R + k^2}, \tag{34}$$

$$B_j = C_j. \tag{35}$$

Therefore, $C_j = \mathcal{A}_{DN}^j C_0$ where $\mathcal{A}_{DN}$ is given in the following theorem.

Theorem 1 (DN iteration)**.** *The amplification factor for the DN iteration is*

$$\mathcal{A}_{DN}(\theta, \beta, \lambda_d, \kappa) = -\frac{1}{\theta}\,\frac{z_R}{z_L}. \tag{36}$$

where (repeating definitions for λ_d, θ and β as an aid to the reader)

$$z_L \stackrel{\text{def}}{=} \sqrt{\frac{3}{2}\frac{1}{\lambda_d} + \kappa^2}, \quad z_R \stackrel{\text{def}}{=} \sqrt{\frac{3}{2}\frac{\beta}{\lambda_d} + \kappa^2}, \quad \kappa \stackrel{\text{def}}{=} kh, \quad \lambda_d = \frac{\Delta t \mathcal{D}_L}{h^2}, \quad \theta = \frac{\mathcal{K}_L}{\mathcal{K}_R}, \quad \beta = \frac{\mathcal{D}_L}{\mathcal{D}_R}. \tag{37}$$

Note that the grid parameter h can be eliminated from (36), but we include it here via the definitions of λ_d and κ for consistency with later results.

The DN iteration converges if $|\mathcal{A}_{DN}| < 1$, and necessary conditions for convergence can be obtained by investigating the limits $\min\left(\frac{3}{2}\frac{1}{\lambda_d}, \frac{3}{2}\frac{\beta}{\lambda_d}\right) \gg \kappa^2$ and $\max\left(\frac{3}{2}\frac{1}{\lambda_d}, \frac{3}{2}\frac{\beta}{\lambda_d}\right) \ll \kappa^2$. It is found that

$$|\mathcal{A}_{DN}| \approx \begin{cases} \frac{1}{\theta}\sqrt{\beta} = \frac{\mathcal{K}_R}{\mathcal{K}_L}\sqrt{\frac{\mathcal{D}_L}{\mathcal{D}_R}} & \text{if } \min\left(\frac{3}{2}\frac{1}{\lambda_d}, \frac{3}{2}\frac{\beta}{\lambda_d}\right) \gg \kappa^2, \\ \frac{1}{\theta} = \frac{\mathcal{K}_R}{\mathcal{K}_L} & \text{if } \max\left(\frac{3}{2}\frac{1}{\lambda_d}, \frac{3}{2}\frac{\beta}{\lambda_d}\right) \ll \kappa^2. \end{cases} \tag{38}$$

In the first case of (38), corresponding to slow variations in y, when the wave number is small, the convergence rate depends on the ratio of the thermal conductivities multiplied by the square root of the ratio of the thermal diffusivities. On the other hand, for the second case of large wave numbers, corresponding to highly oscillatory solutions, the convergence rate depends only on the ratio of the thermal conductivities. Note that switching from the DN to the ND scheme corresponds to replacing θ by $1/\theta$ and β by $1/\beta$ in equation (38) and often either the DN or the ND scheme will be stable. However, it is apparent from the limits in (38) that for some cases such as when $\frac{1}{\theta} < 1$ and $\frac{1}{\theta}\sqrt{\beta} > 1$, it may be that neither the DN nor the ND scheme will be stable. Finally, note that $\mathcal{A}_{DN} \approx 1$ when either $\frac{1}{\theta} \approx 1$ or $\frac{1}{\theta}\sqrt{\beta} \approx 1$. Thus, for these two cases the DN algorithm either converges slowly or not at all.

3.2. Analysis of the optimized Schwarz iteration

As noted above in Section 3.1, one difficult case for the DN iteration is the case of a single material when there is no jump in diffusivities or conductivities across the interface. This is identical to the question of domain decomposition for which there is a well-established literature. In this case, the DN coupling is problematic essentially because the interface conditions are artificially partitioned in a non-symmetric manner (i.e. temperature comes from one side and the heat flux from the other), while the governing equations treat the interface in a symmetric fashion. A more symmetric set of interface conditions can be obtained by taking linear combinations of the two jump conditions in (7) and (8) to yield a pair of Robin-type conditions. An obvious question in this approach is the choice of weighting, which is addressed, for example, in Gander [8]. In addition, it is advantageous to include a domain overlap which is applicable to the case of domain decomposition because the jump conditions hold everywhere in the domain, but which is not obviously applicable to the case of two materials with different thermal properties. Nonetheless it is

useful to understand the optimized Schwarz (OS) iteration for the case of domain decomposition because it ultimately sheds light on the discussion of the CHAMP method to come.

To perform the analysis we again seek solutions to the homogeneous system implied by Algorithm 3 as a superposition of Fourier modes. This leads to a system similar to (28)–(31), but with the interface conditions replaced by

$$\left(\partial_x + \widehat{\mathbf{S}}_L\right) \widehat{T}_L^{(j)}(h,k) = \left(\partial_x + \widehat{\mathbf{S}}_L\right) \widehat{T}_R^{(j-1)}(h,k), \tag{39}$$

$$\left(\partial_x - \widehat{\mathbf{S}}_R\right) \widehat{T}_R^{(j)}(0,k) = \left(\partial_x - \widehat{\mathbf{S}}_R\right) \widehat{T}_L^{(j)}(0,k). \tag{40}$$

It is important to discuss the effect of the domain overlap h in terms of the iteration behavior so that we can compare against the performance of the CHAMP method to be presented below. Substituting the general solution of (28) with physical boundary conditions (31) into the interface conditions (39) and (40) yields

$$C_j \left(\widehat{\mathbf{S}}_L + \sqrt{\eta + k^2}\right) e^{\sqrt{\eta+k^2}h} = B_{j-1} \left(\widehat{\mathbf{S}}_L - \sqrt{\eta + k^2}\right) e^{-\sqrt{\eta+k^2}h}, \tag{41}$$

$$B_j \left(\widehat{\mathbf{S}}_R + \sqrt{\eta + k^2}\right) = C_j \left(\widehat{\mathbf{S}}_R - \sqrt{\eta + k^2}\right), \tag{42}$$

and whence

Theorem 2 (OS iteration)**.** *The amplification factor for the OS iteration is*

$$\mathcal{A}_{OS}(\lambda_d, \kappa) = \frac{\widetilde{\mathbf{S}}_L - z}{\widetilde{\mathbf{S}}_L + z} \cdot \frac{\widetilde{\mathbf{S}}_R - z}{\widetilde{\mathbf{S}}_R + z} e^{-2z}, \tag{43}$$

where

$$z = \sqrt{\frac{3}{2}\frac{1}{\lambda_d} + \kappa^2}, \qquad \widetilde{\mathbf{S}}_L \overset{\text{def}}{=} \widehat{\mathbf{S}}_L h, \quad \widetilde{\mathbf{S}}_R \overset{\text{def}}{=} \widehat{\mathbf{S}}_R h.$$

The exponential term in (43) is the amplification factor of the classical Schwarz iteration, and is introduced from the domain overlap. The two factors preceding the exponential term have a tremendous influence on the performance of the method, and they can be used to minimize $|\mathcal{A}_{OS}|$ for a given problem through the choice of the operators $\widetilde{\mathbf{S}}_m$, $m = L$ or R, which are functions of κ. For example, choosing $\widetilde{\mathbf{S}}_L = \widetilde{\mathbf{S}}_R = z$ causes the amplification factor to vanish identically, i.e. $\mathcal{A}_{OS} = 0$. The resulting algorithm would converge in a single iteration independent of the initial guess, the choice of domain overlap h, and the problem parameter η. This is an optimal result, but in practice one would need the inverse transform of the transmission conditions involving $\widetilde{\mathbf{S}}_m$ from the Fourier domain into the physical domain in order to obtain the transmission operators $\mathbf{S}_m$. Because the optimal choice involves square roots, $\mathbf{S}_m$ would be global operators in y and therefore difficult to wield in practice. On the other hand, if the symbols $\widehat{\mathbf{S}}_m$ are chosen to be polynomials in k, then the operators $\mathbf{S}_m$ consist of only local derivative operators in y. This is the choice made in Gander [8], which leads to a class of optimized Schwarz methods. In this approach $\widetilde{\mathbf{S}}_m$ are chosen to minimize $|\mathcal{A}_{OS}|$ for all possible wavenumbers κ with given λ_d. The first-order transmission conditions take $\widetilde{\mathbf{S}}_m = p_m$, where p_L and p_R are constants, and are simple to analyze and implement. The second-order transmission conditions take $\widetilde{\mathbf{S}}_m = p_m + q_m\kappa^2$, where q_L and q_R are also constants, and are found to give smaller amplification factors but at the cost of introducing the derivative operator ∂_{yy} into $\mathbf{S}_m$ and therefore introducing complexity into the solver. Finally, note that without domain overlap, the exponential term in the amplification factor does not appear in (43), and the iteration does not damp the high wave-number components of the solution very well as shown in Figure 5.

3.3. Development and analysis of the CHAMP iteration

In this section, we extend the optimized Schwarz method discussed in the previous section to a general conjugate-heat-transfer problem where the thermal conductivities and diffusivities jump across the interface. In the case of differing materials, the jump conditions (7) and (8) are applicable only on the interface, which complicates the process of including domain overlap into the scheme. As seen in (43), domain overlap has the important effect of introducing exponential decay for high wavenumber components of the solution. To

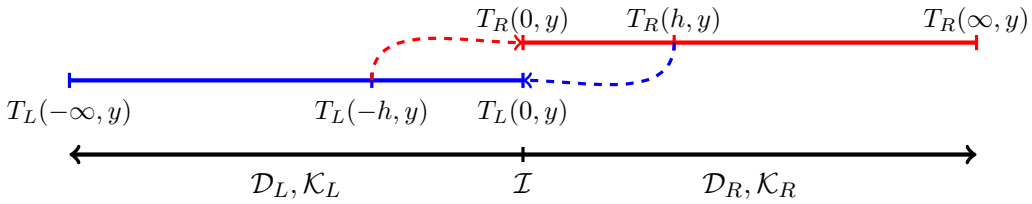

Figure 3: When solving for the left domain T_L, the interface approximation for the CHAMP scheme uses information at an overlapping distance h into the right domain, $T_R(h,y)$, together with jump and compatibility conditions at $\mathcal{I}$. The situation is reversed when solving for the right domain T_R. Incorporating overlapping information improves the stability properties of the scheme.

achieve this effect while enforcing the jump conditions at the interface, we rely on a Taylor series expansion normal to the interface. As presented in Algorithm 3, the new scheme uses a linear combination of generalized Dirichlet and Neumann conditions, and selects the form of the weighting similar to the choice for the OS iteration. The new approach is named the CHAMP (Conjugate Heat transfer Advanced Multi-domain Partitioned) scheme. Broadly speaking, the CHAMP iteration will be shown to converge quickly for any choice of material parameters. In fact the convergence rate is shown to be faster than the DN method even in the limits where the DN scheme performs well, and faster than a typical OS method in the case of domain decomposition.

Although the formulation and analysis is performed with continuous spatial operators, the effect of a computational grid with grid spacing h is introduced by developing the scheme in terms of temperature values $T_L(-h,y)$ and $T_R(h,y)$ that are located a distance h on either side of the interface $x=0$, as shown in Figure 3. To derive the Dirichlet-like portion of the CHAMP condition consider the Taylor series expansion in the x-direction of $T_R(h,y)$ about the point $x=0$:

$$T_R(h,y) = T_R(0,y) + h\partial_x T_R(0,y) + \frac{h^2}{2}\partial_{xx} T_R(0,y) + \mathcal{O}(h^3). \tag{44}$$

Note, that as usual when deriving higher-order accurate schemes, we formally assume that the solutions are as smooth as required for the Taylor series expansions to be valid. Since the current work is concerned with second-order-accurate schemes, the $\mathcal{O}(h^3)$ term in (44) will be dropped[6]. This approximation will be justified later in Section 4.2 and is related to the fact that this value will be used in approximations to derivatives of the temperature. The interface conditions are now used to replace terms involving T_R and its derivatives on the right-hand side of (44) with terms involving T_L and its derivatives. The first two terms can be addressed using the primary interface conditions (7) and (8). To replace the third term involving $\partial_{xx} T_R(0,y)$ we derive an interface compatibility condition by first taking the time derivative of (7) and substituting into (6) to yield

$$\Big[\mathcal{D}\Delta T(0,y)\Big]_{\mathcal{I}} = 0. \tag{45}$$

Since the temperature continuity condition (7) applies for all y we also have

$$\Big[\partial_{yy} T(0,y)\Big]_{\mathcal{I}} = 0. \tag{46}$$

Using (45) and (46), equation (44) is rewritten as

$$\mathbf{D}_{\theta,\beta,h}\left[T_L(0,y)\right] \overset{\text{def}}{=} T_L(0,y) + \theta h \partial_x T_L(0,y) + \frac{h^2}{2}\mathcal{L}_\beta T_L(0,y) = T_R(h,y), \tag{47}$$

where $\mathcal{L}_\beta$ is the operator (26) with $\beta = \frac{\mathcal{D}_L}{\mathcal{D}_R}$, and $\theta = \frac{\mathcal{K}_L}{\mathcal{K}_R}$ as before. The operator $\mathbf{D}_{\theta,\beta,h}\left[T_L(0,y)\right]$ in (47) can be interpreted as a generalized Dirichlet condition for the left domain.

[6]For schemes with higher accuracy more terms in the expansion would need to be retained.

A similar approach is used to derive a generalized Neumann condition for the left domain as follows. First perform the Taylor expansion of $\partial_x T_R(h,y)$ about the interface at $x=0$ as

$$\partial_x T_R(h,y) = \partial_x T_R(0,y) + h\partial_{xx} T_R(0,y) + \mathcal{O}(h^2). \tag{48}$$

Note that the Taylor expansion in (48) is truncated at $\mathcal{O}(h^2)$ as opposed to $\mathcal{O}(h^3)$ as in (44) because here we are dealing directly with the derivative which we require to be second-order accurate (this approximation is justified later in Section 4.2). Again replacing terms involving T_R and its derivative on the right-hand-side with terms involving T_L and its derivatives by applying the interface conditions (7) and (8) along with compatibility conditions (45) and (46) leads to

$$\mathbf{N}_{\theta,\beta,h}\left[T_L(0,y)\right] \stackrel{\text{def}}{=} \theta\partial_x T_L(0,y) + h\,\mathcal{L}_\beta\, T_L(0,y) = \partial_x T_R(h,y). \tag{49}$$

The operator $\mathbf{N}_{\theta,\beta,h}\left[T_L(0,y)\right]$ defines a generalized Neumann condition for the left domain.

Following the approach used in optimized-Schwarz domain-decomposition schemes, (47) and (49) are combined using the weighting operator $\mathbf{S}_L$ to give the new CHAMP interface condition

$$\left(\mathbf{N}_{\theta,\beta,h} + \mathbf{S}_L\mathbf{D}_{\theta,\beta,h}\right)\left[T_L(0,y)\right] = \left(\partial_x + \mathbf{S}_L\right) T_R(h,y), \tag{50}$$

to be applied to the left domain. Analogously, the generalized Robin condition

$$\left(\mathbf{N}_{\frac{1}{\theta},\frac{1}{\beta},-h} - \mathbf{S}_R\mathbf{D}_{\frac{1}{\theta},\frac{1}{\beta},-h}\right)\left[T_R(0,y)\right] = \left(\partial_x - \mathbf{S}_R\right) T_L(-h,y), \tag{51}$$

is the CHAMP interface condition to be applied to the right domain.

The CHAMP conditions (50)–(51) can be used in Algorithm 1. The convergence of the inner iteration loop can be analyzed as before by first Fourier transforming the equation in the y-direction then seeking solutions to the transformed heat equation (28) together with the interface conditions

$$\left(\widehat{\mathbf{N}}_{\theta,\beta,h} + \widehat{\mathbf{S}}_L\widehat{\mathbf{D}}_{\theta,\beta,h}\right)\left[\widehat{T}_L^{(j)}(0,k)\right] = \left(\partial_x + \widehat{\mathbf{S}}_L\right)\widehat{T}_R^{(j-1)}(h,k), \tag{52}$$

$$\left(\widehat{\mathbf{N}}_{\frac{1}{\theta},\frac{1}{\beta},-h} - \widehat{\mathbf{S}}_R\widehat{\mathbf{D}}_{\frac{1}{\theta},\frac{1}{\beta},-h}\right)\left[\widehat{T}_R^{(j)}(0,k)\right] = \left(\partial_x - \widehat{\mathbf{S}}_R\right)\widehat{T}_L^{(j)}(-h,k), \tag{53}$$

where the Fourier transformed CHAMP operators are

$$\widehat{\mathbf{D}}_{\theta,\beta,h}\left[\widehat{T}_L(0,k)\right] \stackrel{\text{def}}{=} \widehat{T}_L(0,k) + \theta h\partial_x\widehat{T}_L(0,k) + \frac{h^2}{2}\,\widehat{\mathcal{L}}_\beta\,\widehat{T}_L(0,k), \tag{54}$$

$$\widehat{\mathbf{N}}_{\theta,\beta,h}\left[\widehat{T}_L(0,k)\right] \stackrel{\text{def}}{=} \theta\partial_x\widehat{T}_L(0,k) + h\,\widehat{\mathcal{L}}_\beta\,\widehat{T}_L(0,k), \tag{55}$$

with

$$\widehat{\mathcal{L}}_\beta \stackrel{\text{def}}{=} \beta\partial_{xx} - (\beta-1)k^2.$$

Substituting the general solutions of the heat equations (28) and physical boundary conditions (31) into the CHAMP interface conditions (52)–(53) gives

$$\left(\theta z_L + z_R^2 + \widetilde{\mathbf{S}}_L\left(1 + \theta z_L + \frac{1}{2}z_R^2\right)\right) C_j = \left(-z_R + \widetilde{\mathbf{S}}_L\right) e^{-z_R} B_{j-1}, \tag{56}$$

$$\left(\frac{1}{\theta}z_R + z_L^2 + \widetilde{\mathbf{S}}_R\left(1 + \frac{1}{\theta}z_R + \frac{1}{2}z_L^2\right)\right) B_j = \left(-z_L + \widetilde{\mathbf{S}}_R\right) e^{-z_L} C_j, \tag{57}$$

where

$$z_L = \sqrt{\frac{3}{2}\frac{1}{\lambda_d} + \kappa^2}, \qquad z_R = \sqrt{\frac{3}{2}\frac{\beta}{\lambda_d} + \kappa^2},$$

and $\widetilde{\mathbf{S}}_L = h\,\widehat{\mathbf{S}}_L$ and $\widetilde{\mathbf{S}}_R = h\,\widehat{\mathbf{S}}_R$ as before. This leads to the following

Theorem 3 (CHAMP iteration)**.** *The amplification factor for the CHAMP iteration is*

$$\mathcal{A}_{CI}(\theta,\beta,\lambda_d,\kappa) = \frac{\left(-z_R+\widetilde{\mathbf{S}}_L\right)e^{-z_R}}{\theta z_L + z_R^2 + \widetilde{\mathbf{S}}_L\left(1+\theta z_L+\frac{1}{2}z_R^2\right)} \cdot \frac{\left(-z_L+\widetilde{\mathbf{S}}_R\right)e^{-z_L}}{\frac{1}{\theta}z_R + z_L^2 + \widetilde{\mathbf{S}}_R\left(1+\frac{1}{\theta}z_R+\frac{1}{2}z_L^2\right)}, \tag{58}$$

where

$$\lambda_d = \frac{\Delta t \mathcal{D}_L}{h^2}, \qquad \kappa = kh, \qquad \theta = \frac{\mathcal{K}_L}{\mathcal{K}_R}, \qquad \beta = \frac{\mathcal{D}_L}{\mathcal{D}_R}.$$

Note that $\mathcal{A}_{CI}$ is a function of the four dimensionless parameters κ, λ_d, θ and β.

The exponential terms e^{-z_R} and e^{-z_L} in the numerator of $\mathcal{A}_{CI}$ indicate that the CHAMP conditions benefit from an effective overlap of width h, similar to OS schemes for DD problems with explicit overlap, even though there is no overlap in the original formulation of the CHT interface conditions. Also similar to OS, the factors multiplying the exponential terms have a significant influence on the performance of the iteration. The amplification factor vanishes identically for the choice $\widetilde{\mathbf{S}}_m = z_m$, $m = L, R$, and thus the scheme would converge in one iteration independent of the initial guess or problem parameters. As in OS, however, this choice would yield a non-local operator in physical space after applying the inverse Fourier transform. Seeking only local operators in physical space is akin to seeking $\widetilde{\mathbf{S}}_m$ as polynomials in κ, and to simplify the analysis and implementation we consider $\widetilde{\mathbf{S}}_L = p_L$ and $\widetilde{\mathbf{S}}_R = p_R$, where p_L and p_R are positive constants.

Prior to discussing the determination of specific values for p_L and p_R, let begin by comparing properties of the CHAMP iteration to those of the OS and DN iterations. First consider the case of domain decomposition when $\mathcal{D}_L = \mathcal{D}_R$, $\mathcal{K}_L = \mathcal{K}_R$ and $\theta = 1$, which implies $z_L = z_R = z$. Let us also assume that the same parameters $\widetilde{\mathbf{S}}_m$, $m = L, R$, are used for both the OS and CHAMP schemes and that $\widetilde{\mathbf{S}}_L \geq 0$ and $\widetilde{\mathbf{S}}_R \geq 0$. In this case (assuming an overlap width of h for the DN scheme)

$$|\mathcal{A}_{DN}| = e^{-2z}, \tag{59}$$

$$|\mathcal{A}_{OS}| = \left|\frac{\widetilde{\mathbf{S}}_L - z}{\widetilde{\mathbf{S}}_L + z}\right| \left|\frac{\widetilde{\mathbf{S}}_R - z}{\widetilde{\mathbf{S}}_R + z}\right| e^{-2z}, \tag{60}$$

$$|\mathcal{A}_{CI}| = \left|\frac{\widetilde{\mathbf{S}}_L - z}{\widetilde{\mathbf{S}}_L + z + z^2 + \widetilde{\mathbf{S}}_L\left(z+\frac{1}{2}z^2\right)}\right| \left|\frac{\widetilde{\mathbf{S}}_R - z}{\widetilde{\mathbf{S}}_R + z + z^2 + \widetilde{\mathbf{S}}_R\left(z+\frac{1}{2}z^2\right)}\right| e^{-2z}. \tag{61}$$

Since $z > 0$ and $\widetilde{\mathbf{S}}_m \geq 0$ it follows that

$$|\mathcal{A}_{CI}| < |\mathcal{A}_{OS}| < |\mathcal{A}_{DN}|.$$

Thus the convergence rate of the CHAMP iteration is faster than that for OS, and both converge faster than DN.

Secondly, consider the usual CHT situation where material parameters jump across the interface. We argue that there always exist some scalar values for the weights $\widetilde{\mathbf{S}}_L = p_L$ and $\widetilde{\mathbf{S}}_R = p_R$ so that the CHAMP iteration converges. To see this, it is useful to separately consider the iteration amplification factors for the CHAMP scheme with weightings chosen to yield only the Dirichlet or Neumann portions in (50) and (51). We refer to these amplification factors as $\mathcal{A}_{CH,D}$ and $\mathcal{A}_{CH,N}$ respectively, and they can be expressed as

$$\mathcal{A}_{CI,D} = \frac{e^{-(z_R+z_L)}}{\left(1+\theta z_L+\frac{1}{2}z_R^2\right)\left(1+\frac{1}{\theta}z_R+\frac{1}{2}z_L^2\right)}, \tag{62}$$

$$\mathcal{A}_{CI,N} = \frac{e^{-(z_R+z_L)}}{1+\theta\frac{z_L^2}{z_R}+\frac{1}{\theta}\frac{z_R^2}{z_L}+z_L z_R}. \tag{63}$$

Note that $e^{-z_m} < 1$, since z_m, $m = L, R$, are real and positive, and furthermore the denominators of $\mathcal{A}_{CI,D}$ and $\mathcal{A}_{CI,N}$ are always greater than one. Therefore, it follows that $|\mathcal{A}_{CI,D}| < 1$ and $|\mathcal{A}_{CI,N}| < 1$. Thus, there exists a set of weights, corresponding to either the pure Dirichlet or the pure Neumann portions of (50)

CHAMP iteration: $\beta = 1$, $\lambda_d = 10^6$			
θ	p_L	p_R	$\mathcal{A}^*_{CI}$
1.00e-02	9.17e-02	1.18e-03	7.66e-03
4.64e-02	7.43e-02	1.76e-03	3.20e-02
2.15e-01	5.90e-02	1.81e-03	1.33e-01
1.00e+00	2.17e-03	3.31e-02	3.48e-01
4.64e+00	1.83e-03	5.89e-02	1.33e-01
2.15e+01	1.76e-03	7.43e-02	3.20e-02
1.00e+02	1.18e-03	9.17e-02	7.66e-03

CHAMP iteration: $\beta = 1$, $\theta = 1$			
λ_d	p_L	p_R	$\mathcal{A}^*_{CI}$
2.00e+07	6.57e-04	1.94e-02	4.80e-01
1.00e+07	8.43e-04	2.09e-02	4.40e-01
5.00e+06	1.11e-03	2.40e-02	4.10e-01
2.50e+06	1.45e-03	2.77e-02	3.83e-01
1.25e+06	2.00e-03	3.20e-02	3.59e-01
6.25e+05	2.50e-03	3.59e-02	3.32e-01
3.12e+05	3.46e-03	4.22e-02	3.00e-01

CHAMP iteration: $\theta = 1$, $\lambda_d = 10^6$			
β	p_L	p_R	$\mathcal{A}^*_{CI}$
1.00e-02	2.88e-02	1.68e-03	3.75e-01
4.64e-02	3.00e-02	1.75e-03	3.67e-01
2.15e-01	3.12e-02	1.89e-03	3.61e-01
1.00e+00	2.17e-03	3.31e-02	3.48e-01
4.64e+00	3.60e-03	4.32e-02	2.96e-01
2.15e+01	6.64e-03	5.76e-02	2.40e-01
1.00e+02	1.28e-02	8.16e-02	1.77e-01

Table 1: Optimized amplification factor $\mathcal{A}^*_{CI}$ for the CHAMP iterations and corresponding values of p_m for various choices of the dimensionless parameters $\theta = \frac{\mathcal{K}_L}{\mathcal{K}_R}$, $\beta = \frac{\mathcal{D}_L}{\mathcal{D}_R}$, and $\lambda_d = \frac{\Delta t \mathcal{D}_L}{h^2}$.

and (51), such that the CHAMP iteration converges for any set of material parameters, grid spacings and time step. In practice, however, more rapid convergence can be achieved through more careful selection of p_m. As an aside, the optimal choice of p_m for rapid convergence is especially important in the context of the CHAMP time-stepping scheme so that as few iterations per time-step as possible are required.

We now return the problem of determining optimal values for the coefficients p_L and p_R; these values will depend on the problem parameters θ, β and λ_d. In general, we seek values for p_L and p_R to minimize the magnitude of the amplification factor $|\mathcal{A}_{CI}|$ for all κ. This can be expressed mathematically as finding the solution to the minimax problem

$$\mathcal{A}^*_{CI} \stackrel{\text{def}}{=} \min_{p_L>0,\, p_R>0} \left[\max_{\kappa_{\min} \le \kappa \le \kappa_{\max}} |\mathcal{A}_{CI}| \right], \tag{64}$$

$$[p_L, p_R] \stackrel{\text{def}}{=} \operatorname*{argmin}_{p_L>0,\, p_R>0} \left[\max_{\kappa_{\min} \le \kappa \le \kappa_{\max}} |\mathcal{A}_{CI}| \right]. \tag{65}$$

The parameter $\kappa = kh$ is restricted to the range $[\kappa_{\min}, \kappa_{\max}] = [-\pi, \pi]$. This restricts the Fourier modes k under consideration to the range $[-\pi/h, \pi/h]$, thus approximating the largest value for k that would occur in a fully discrete approximation. Since the highest frequencies are strongly damped by the CHAMP iteration, they do not strongly affect the choice of p_m and thus this cutoff is a reasonable approximation in practice. Furthermore, since $\mathcal{A}_{CI}$ is only function of κ^2, the search space may be further restricted to $\kappa \in [0, \pi]$. In our implementation the solution to the minimax problem in (65) is first found using the DIRECT algorithm for global optimization [21]. Those results are then used as initial conditions for the local BOBYQA algorithm [22], where the objective function is $\max_{\kappa_{\min} < \kappa < \kappa_{\max}} |\mathcal{A}_{CI}|$ subject to bounds $p_m \in [z_m(k=0), z_m(k=\pi)]$ for $m = L, R$ where z_m was defined in (37). This optimization procedure is implemented with the software package NLopt [23]. Results obtained using this procedure are shown in Tables 1 which give numerical values for the optimized amplification factor and associated p_m for a range of relevant values for the dimensionless parameters θ, β, and λ_d.

Figure 4 shows the behavior of the optimized iteration amplification factor for the CHAMP scheme,

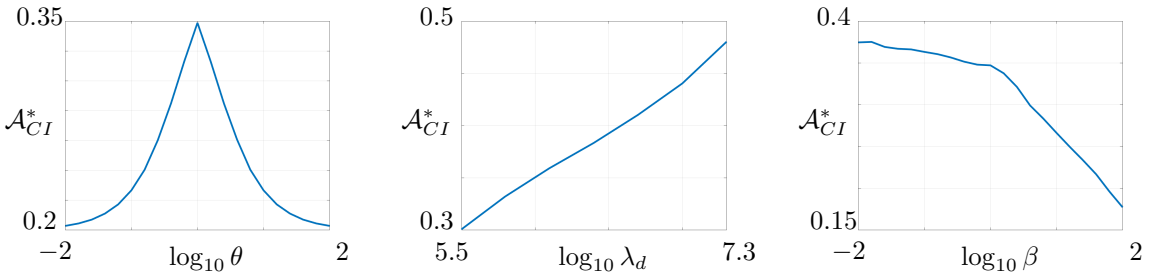

Figure 4: Magnitude of the optimized amplification factor, $\mathcal{A}^*_{CI}$, for CHAMP iterations, for various choices of parameters $\theta = \frac{\mathcal{K}_L}{\mathcal{K}_R}$, $\beta = \frac{\mathcal{D}_L}{\mathcal{D}_R}$, and $\lambda_d = \frac{\Delta t \mathcal{D}_L}{h^2}$. Left: Optimized $\mathcal{A}_{CI}$ as a function of θ for $\lambda_d = 10^6$ and $\beta = 1$. Middle: Optimized $\mathcal{A}_{CI}$ as a function of λ_d for $\beta = 1$ and $\theta = 1$. Right: Optimized $\mathcal{A}_{CI}$ as a function of β for $\lambda_d = 10^6$ and $\theta = 1$.

$\mathcal{A}^*_{CI}$, as the parameters λ_d, θ and β vary. The left plot shows $\mathcal{A}^*_{CI}$ for varying θ between 10^{-2} and 10^2 with $\lambda_d = 10^6$ and $\beta = 1$ held fixed. We observe that the largest value of $\mathcal{A}^*_{CI}$ occurs at $\theta = 1$ where the conductivities of the two domains are equal. Also, the rate of convergence improves ($\mathcal{A}^*_{CI}$ decreases) as the ratio of the thermal conductivities becomes large or small, similar to the behavior for the DN iteration. The plot in the middle illustrates the behavior of $\mathcal{A}^*_{CI}$ as λ_d varies with the other two parameters held fixed. Here we see that $\mathcal{A}^*_{CI}$ increases as λ_d increases. We note that increasing λ_d corresponds to increasing Δt (at fixed h) or decreasing h (at fixed Δt); the converge rate thus degrades for a larger time-step or a smaller overlap width h. The right plots shows the behavior of $\mathcal{A}^*_{CI}$ as β varies. Since β appears in the formula for $\mathcal{A}_{CI}$ in (58) only as a scaling of λ_d through the definition of z_R, the effect of varying β is similar to that of varying λ_d. An increase in β, for example, amounts to a decrease in λ_d for the right domain, and we see that $\mathcal{A}^*_{CI}$ decreases as expected.

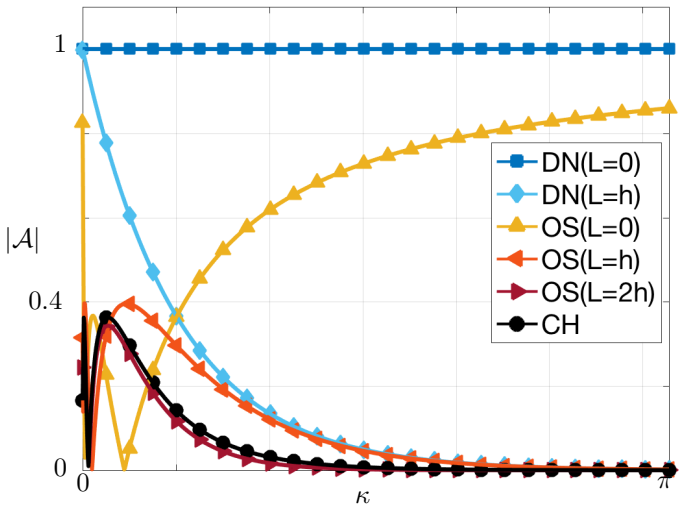

Figure 5: A comparison of the convergence rates of different schemes for the iterative solution of the domain decomposition problem (i.e. equal material properties). The magnitude of the amplification factor $\mathcal{A}$ for iterations, as a function of the normalized wave-number κ, for the DN method, the OS method (with domain overlap 0, h and $2h$), and the CHAMP method with $\lambda_d = \frac{\Delta t \mathcal{D}_L}{h^2} = 10^6$, $\beta = \frac{\mathcal{D}_L}{\mathcal{D}_R} = 1$ and $\theta = \frac{\mathcal{K}_L}{\mathcal{K}_R} = 1$. The OS and CHAMP results use their respective optimal values of p_m. The overall convergence rate is determined by the worst case amplification factor over all κ.

Amplification factors for the DN, OS and CHAMP schemes as functions of κ are shown in Figure 5 for a domain decomposition problem to illustrate and compare the behaviors of the three schemes. The results are shown for the difficult case $\lambda_d = 10^6$, $\beta = 1$ and $\theta = 1$, and p_L and p_R are calculated from the optimization

problem in (65) for the CHAMP method, and the corresponding optimization problem for the case of OS. These results confirm that in the case of uniform materials the CHAMP iteration converges rapidly while the traditional DN iteration converges very slowly (ignoring mode $\kappa = 0$). In addition, the convergence rate for the CHAMP method (and OS with overlap) is slower at smaller wave numbers where the exponential decay is not significant, while it is very fast at higher wave numbers where the exponential term leads to very small values of the amplification factors for both OS with overlap and CHAMP. Finally note that the CHAMP iteration is almost as good as the OS method with an overlap of width $2h$. This behavior can be partially explained by examining the forms (60) and (61) for $\mathcal{A}_{OS}$ and $\mathcal{A}_{CI}$. For $\lambda_d = 10^6$, $z_L = z_R \approx \kappa$, while $\widetilde{\mathbf{S}}_L = \epsilon_L$ and $\widetilde{\mathbf{S}}_R = \epsilon_R$ for some small $\epsilon_L \ll 1$ and $\epsilon_R \ll 1$ (the values of $\mathcal{A}_{OS}$ and $\mathcal{A}_{CI}$ are zero when $z = \widetilde{\mathbf{S}}_L$ or $z = \widetilde{\mathbf{S}}_R$ and this occurs very near $\kappa = 0$ as seen in the figure.). In the region where κ is small, but not too small, i.e. for $\epsilon_m < \kappa < 1$, the behaviors of the amplification factors are approximately given by

$$
\begin{aligned}
|\mathcal{A}_{OS}(h)| &\approx \frac{(\epsilon_L - \kappa)(\epsilon_R - \kappa)}{(\epsilon_L + \kappa)(\epsilon_R + \kappa)} e^{-2\kappa} \approx e^{-2\kappa}, \\
|\mathcal{A}_{OS}(2h)| &\approx e^{-4\kappa}, \\
|\mathcal{A}_{CI}| &\approx \frac{\kappa^2}{\kappa^2(1+\kappa)^2} e^{-2\kappa} \approx \frac{1}{(1+\kappa)^2} e^{-2\kappa} \approx \frac{1}{(e^\kappa)^2} e^{-2\kappa} \approx e^{-4\kappa}.
\end{aligned}
$$

We see that the extra terms in the denominator of (61) contribute to the decay of $|\mathcal{A}_{CI}|$ as κ increases and this decay is roughly similar to $|\mathcal{A}_{OS}(2h)|$ which has twice the overlap.

One final note with respect to the behavior of the DN, OS and CHAMP iterations concerns the original choice of time integration scheme. Changing the time integrator will indeed affect the iteration convergence rates, but those effects are rather minor and easily analyzed. For example suppose the BDF integrator is replaced by Crank-Nicolson (CN), another commonly-used time-integration method for this problem. The iteration problem in this case replaces (16) with

$$
\frac{1}{\frac{1}{2}\mathcal{D}_m \Delta t} T_m^{(j)} - \Delta T_m^{(j)} = \tilde{F}_m, \qquad \text{for } \mathbf{x} \in \Omega_m, \tag{66}
$$

where

$$
\tilde{F}_m \stackrel{\text{def}}{=} \frac{1}{\frac{1}{2}\mathcal{D}_m \Delta t} T_m^n + \Delta T_m^n.
$$

The amplification factors for the case of CN are therefore similar to those for BDF with a slight modification to the definitions of z_L and z_R for DN and CHAMP, and z for OS, where λ_d is replaced by $4\lambda_d/3$.

4. Analysis of the CHAMP time-stepping scheme

We now perform an analysis of the partitioned CHT solver given in Algorithm 1. The algorithm includes the general operators, $\mathcal{B}_L$, $\mathcal{B}_{LR}$, $\mathcal{B}_R$ and $\mathcal{B}_{RL}$, in the partitioned interface conditions (see steps 10 and 14) which we take to be the CHAMP interface conditions in (24) and (25). These interface conditions are applied iteratively in the "**for** j" loop of the partitioned CHT solver for each time step. Having considered the convergence behavior of the CHAMP iteration in isolation in the previous section, our goal now is to examine the stability and accuracy of the partitioned solver with the embedded CHAMP interface conditions. There are two basic issues that require some attention. The first concerns choosing the appropriate number of sub-time-step iterations, N_{si}. If, on the one hand, the number of sub-time-step iterations given by N_{si} is taken to be large so that the CHAMP iteration converges (to some small tolerance), then the time-stepping scheme effectively becomes a monolithic scheme for (12)–(15), and the stability and accuracy of scheme no longer depend on the CHAMP iteration so long as it converges. For a partitioned scheme, on the other hand, the objective is to take N_{si} as small as possible, and perhaps even equal to one so that no sub-time-step iterations are taken and the CHAMP interface conditions are used once for each subdomain. For this case, the stability and accuracy of the scheme with a small and fixed number of sub-iterations becomes important. Furthermore, when N_{si} is taken to be small, a second important consideration is the initial guess for the sub-iterations. A typical strategy, and the one employed here, is to extrapolate the necessary values near the interface from the corresponding values at previous time steps. A sufficiently high-order extrapolation

formula is needed to maintain accuracy of the time-stepping scheme, second-order accuracy for the present scheme, but this approach can lead to instabilities as discussed in Peet and Fischer [10]. Additional sub-time-step iterations can be used to suppress the instabilities, but the goal is to keep N_{si} small for efficiency of the partitioned solver.

4.1. Stability of the un-iterated CHAMP time-stepping scheme

Let us consider the behavior of the *un-iterated* CHAMP time-stepping scheme with $N_{\text{si}} = 1$, and with an appropriate extrapolation formula for second-order accuracy. The scheme is given by

$$\widetilde{T}_R^{n+1} = 3T_R^n - 3T_R^{n-1} + T_R^{n-2}, \qquad \text{for } \mathbf{x} \in \Omega_R, \tag{67}$$

$$T_m^{n+1} - \frac{4}{3}T_m^n + \frac{1}{3}T_m^{n-1} = \frac{2\Delta t}{3}\mathcal{D}_m \Delta T_m^{n+1}, \qquad \text{for } \mathbf{x} \in \Omega_m, \tag{68}$$

$$\left(\mathbf{N}_{\theta,\beta,h} + \mathbf{S}_L \mathbf{D}_{\theta,\beta,h}\right)\left[T_L^{n+1}(0,y)\right] = \left(\partial_x + \mathbf{S}_L\right)\widetilde{T}_R^{n+1}(h,y), \qquad \text{for } y \in [0,2\pi] \tag{69}$$

$$\left(\mathbf{N}_{\frac{1}{\theta},\frac{1}{\beta},-h} - \mathbf{S}_R \mathbf{D}_{\frac{1}{\theta},\frac{1}{\beta},-h}\right)\left[T_R^{n+1}(0,y)\right] = \left(\partial_x - \mathbf{S}_R\right)T_L^{n+1}(-h,y), \qquad \text{for } y \in [0,2\pi] \tag{70}$$

$$T_L^{n+1}(-\infty,y) = 0, \qquad T_R^{n+1}(\infty,y) = 0, \qquad \text{for } y \in [0,2\pi] \tag{71}$$

along with 2π periodicity in y.

The time-step begins with an application of a third-order extrapolation in time given in (67) for the domain on the right. This extrapolation provides the necessary values for the right-hand side of the CHAMP interface condition in (69), which can then be used with the far-field boundary conditions in (71) to solve the Helmholtz equation in (68) with $m = L$. The solution in the left domain can now be used to compute the right-hand side of the CHAMP interface conditions in (70), and the solution in the right domain can by found by solving (68) with $m = R$. This procedure completes a time step of the un-iterated CHAMP scheme.

To analyze the time-stepping scheme given by (67)–(71), we again perform a Fourier expansion in y to give

$$\widehat{\widetilde{T}}_R^{n+1} = 3\widehat{T}_R^n - 3\widehat{T}_R^{n-1} + \widehat{T}_R^{n-2}, \tag{72}$$

$$\widehat{T}_m^{n+1} - \frac{4}{3}\widehat{T}_m^n + \frac{1}{3}\widehat{T}_m^{n-1} = \frac{2\Delta t}{3}\mathcal{D}_m\left(\partial_{xx}\widehat{T}_m^{n+1} - k^2\widehat{T}_m^{n+1}\right), \tag{73}$$

$$\left(\widehat{\mathbf{N}}_{\theta,\beta,h} + \widehat{\mathbf{S}}_L\widehat{\mathbf{D}}_{\theta,\beta,h}\right)\left[\widehat{T}_L^{n+1}(0,k)\right] = \left(\partial_x + \widehat{\mathbf{S}}_L\right)\widehat{\widetilde{T}}_R^{n+1}(h,k), \tag{74}$$

$$\left(\widehat{\mathbf{N}}_{\frac{1}{\theta},\frac{1}{\beta},-h} - \widehat{\mathbf{S}}_R\widehat{\mathbf{D}}_{\frac{1}{\theta},\frac{1}{\beta},-h}\right)\left[\widehat{T}_R^{n+1}(0,k)\right] = \left(\partial_x - \widehat{\mathbf{S}}_R\right)\widehat{T}_L^{n+1}(-h,k), \tag{75}$$

$$\widehat{T}_L^{n+1}(-\infty,k) = 0, \qquad \widehat{T}_R^{n+1}(\infty,k) = 0. \tag{76}$$

These differential-difference equations can be solved by seeking solutions in the form of normal modes

$$\widehat{T}_L^n = A^n e^{\zeta_L x}, \qquad \widehat{T}_R^n = A^n e^{-\zeta_R x},$$

where A is the amplification factor of the time-stepping scheme. The scheme is stable in the sense of Godunov-Ryabenkii provided there are no nontrivial solutions to the homogeneous equations (72)–(76) with $|A| > 1$. Substitution of the normal-mode ansatz into (73) results in two possible roots for both ζ_L and ζ_R given by

$$\zeta_m = \pm\sqrt{\frac{1}{\mathcal{D}_m\Delta t}\frac{3A^2 - 4A + 1}{2A^2} + k^2}, \qquad m = L \text{ or } R. \tag{77}$$

The fact that a scheme based on (73) solved in a single domain with periodic boundary conditions in x is stable is encompassed in the following lemma.

Lemma 1. *Consider ζ_m and A satisfying (77). If ζ_m is pure imaginary, then $|A| \leq 1$. Furthermore $|A| = 1$ only when $\zeta_m = 0$ and $k = 0$, in which case $A = 1$ is a simple root.*

Proof. Let ζ_m be pure imaginary, $\zeta_m = i\alpha$, $\alpha \in \mathbb{R}$. Equation (77) can be written as a polynomial of degree two in A,

$$(3-c)\,A^2 - 4A + 1 = 0,$$

with

$$c = -2(\alpha^2 + k^2)\mathcal{D}_m \Delta t.$$

It follows that $c \le 0$ and $c = 0$ iff $\alpha = k = 0$, in which case $A = 1$ or $A = 1/3$. Otherwise if $c < 0$, then we want to show $|A| < 1$. From the theory of von Neumann polynomials, Chapter 4.3 in [24], $|A| < 1$ if and only if

$$4 < |4 - c| \quad \text{and} \quad 1 < |3 - c|\,. \tag{78}$$

These two conditions do hold when $c < 0$ and thus $|A| < 1$. □

Lemma 1 shows that all solutions to (72)–(76) corresponding to pure imaginary values of ζ_m are stable. Let us therefore reduce the analysis to the situation when ζ_m has a nonzero real part. For this case one solution ζ_m from (77) has a positive real part and the other has a negative real part. To satisfy the far-field boundary conditions in (76), only one of the two roots in (77) is retained for each domain, leading to the solutions of the form

$$\widehat{T}_L^n = c_L A^n e^{\zeta_L x}, \qquad \widehat{T}_R^n = c_R A^n e^{-\zeta_R x}, \tag{79}$$

where the principal branch of the square root in (77) has been chosen so that the sign of the real part of ζ_m is positive. Substituting the solutions in (79) back into the CHAMP interface conditions (74)–(75), and using the extrapolation formula (72) yields

$$\begin{aligned}
c_L A^3 \left(\theta\zeta_L + h\left(\beta\zeta_L^2 - (\beta-1)\,k^2\right) + \widehat{\mathbf{S}}_L\left(1 + \theta h\zeta_L + \frac{h^2}{2}\left(\beta\zeta_L^2 - (\beta-1)\,k^2\right)\right)\right) \\
= c_R\left(3A^2 - 3A + 1\right)\left(-\zeta_R + \widehat{\mathbf{S}}_L\right)e^{-\zeta_R h}, \\
c_R\left(\frac{1}{\theta}\zeta_R + h\left(\frac{1}{\beta}\zeta_R^2 - \left(\frac{1}{\beta} - 1\right)k^2\right) + \widehat{\mathbf{S}}_R\left(1 + \frac{1}{\theta}h\zeta_R + \frac{h^2}{2}\left(\frac{1}{\beta}\zeta_R^2 - \left(\frac{1}{\beta} - 1\right)k^2\right)\right)\right) \\
= c_L\left(-\zeta_L + \widehat{\mathbf{S}}_R\right)e^{-\zeta_L h}.
\end{aligned}$$

The two equations above can be written as a homogeneous system of equations for c_L and c_R. Nontrivial solutions of the system exist only if the determinant of the coefficient matrix is zero. This leads to:

Theorem 4 (CHAMP time-stepping stability condition)**.** *The un-iterated CHAMP time-stepping algorithm given by (67)–(71) is stable in the sense of Godunov-Ryabenkii provided there are no roots A with $|A| > 1$ to*

$$G(A) \equiv \frac{A^3}{3A^2 - 3A + 1} - \frac{\left(-\widetilde{\zeta}_R + \widetilde{\mathbf{S}}_L\right)e^{-\widetilde{\zeta}_R}}{\theta\widetilde{\zeta}_L + \widetilde{\zeta}_R^2 + \widetilde{\mathbf{S}}_L\left(1 + \theta\widetilde{\zeta}_L + \frac{1}{2}\widetilde{\zeta}_R^2\right)} \cdot \frac{\left(-\widetilde{\zeta}_L + \widetilde{\mathbf{S}}_R\right)e^{-\widetilde{\zeta}_L}}{\frac{1}{\theta}\widetilde{\zeta}_R + \widetilde{\zeta}_L^2 + \widetilde{\mathbf{S}}_R\left(1 + \frac{1}{\theta}\widetilde{\zeta}_R + \frac{1}{2}\widetilde{\zeta}_L^2\right)} = 0, \tag{80}$$

where

$$\widetilde{\zeta}_L = h\zeta_L = \sqrt{\frac{1}{\lambda_d}\,\frac{3A^2 - 4A + 1}{2A^2} + \kappa^2}, \qquad \widetilde{\zeta}_R = h\zeta_R = \sqrt{\frac{\beta}{\lambda_d}\,\frac{3A^2 - 4A + 1}{2A^2} + \kappa^2}, \tag{81}$$

and $\widetilde{\mathbf{S}}_L = h\,\widehat{\mathbf{S}}_L$ and $\widetilde{\mathbf{S}}_R = h\,\widehat{\mathbf{S}}_R$. The non-dimensional quantities θ, β, λ_d and κ are given in Theorem 3.

Theorem 4 provides a condition for which the time-stepping algorithm is stable. The problem becomes specifying the operators $\widetilde{\mathbf{S}}_m$ such that this condition is met, i.e. that (80) has no solutions with $|A| > 1$. As before, we consider the simple forms $\widetilde{\mathbf{S}}_L = p_L$ and $\widetilde{\mathbf{S}}_R = p_R$ with $p_m > 0$, and in principle we only need to find values for p_L and p_R such that all roots of $G(A)$ have $|A| < 1$. In practice, however, we choose to find p_L and p_R that minimize the largest value of $|A|$, where A is a solution of (80). The motivation is to obtain values for p_L and p_R that make the stability of the time-stepping algorithm more robust to perturbations (e.g. when applied later to problems on curvilinear grids where the theory only applies approximately).

The problem of finding p_L and p_R that minimize the largest value of $|A|$ is difficult since $G(A)$ is a transcendental function of A. There appears to be no closed-form solution of (80) for A as a function of θ, β, κ and λ_d. In addition, root-finding methods cannot be guaranteed to find all solutions to (80), and therefore unstable roots could potentially be missed in the optimization procedure. Indeed, even the number roots of $G(A)$ is unknown.

To address these difficulties, we consider instead the minimization problem for a nearby function whose roots can be found unambiguously. Using quadratic Taylor polynomial approximations for the exponential terms in $G(A)$ assuming $|\widetilde{\zeta}_m| \ll 1$[7], and setting $\widetilde{\mathbf{S}}_m = p_m$ gives

$$\tilde{G}(A) \equiv \frac{A^3}{3A^2 - 3A + 1} - \frac{\left(-\widetilde{\zeta}_R + p_L\right)\left(1 - \widetilde{\zeta}_R + \frac{1}{2}\widetilde{\zeta}_R^2\right)}{\theta\widetilde{\zeta}_L + \widetilde{\zeta}_R^2 + p_L\left(1 + \theta\widetilde{\zeta}_L + \frac{1}{2}\widetilde{\zeta}_R^2\right)} \cdot \frac{\left(-\widetilde{\zeta}_L + p_R\right)\left(1 - \widetilde{\zeta}_L + \frac{1}{2}\widetilde{\zeta}_L^2\right)}{\frac{1}{\theta}\widetilde{\zeta}_R + \widetilde{\zeta}_L^2 + p_R\left(1 + \frac{1}{\theta}\widetilde{\zeta}_R + \frac{1}{2}\widetilde{\zeta}_L^2\right)} = 0. \quad (82)$$

The function $\tilde{G}(A)$ can be readily manipulated into a polynomial in the variables A, $\widetilde{\zeta}_L$ and $\widetilde{\zeta}_R$. This polynomial can be combined with polynomials obtained by squaring the definitions for $\widetilde{\zeta}_L$ and $\widetilde{\zeta}_R$ in (81) to obtain a polynomial system. The roots of this polynomial system can be found for given values of λ_d, θ and β using classical techniques such as determining the eigenvalues of a companion matrix. Note that the validity of these roots must be checked in the original equations since spurious roots may have been introduced when the expressions for $\widetilde{\zeta}_L$ and $\widetilde{\zeta}_R$ in (81) were squared.

Let $\mathcal{A}_{CT}(\theta, \beta, \lambda_d, \kappa)$ denote the valid roots to the polynomial system determined from (81) and (82). As for the case of the CHAMP iteration in isolation, we wish to find values for p_L and p_R to minimize $|\mathcal{A}_{CT}|$ over a range of κ. Let $\mathcal{A}^*_{CT}$ denote this optimal value, i.e.

$$\begin{aligned} \mathcal{A}^*_{CT} &\stackrel{\text{def}}{=} \min_{p_L>0,\, p_R>0} \left[\max_{\kappa_{\min}\le\kappa\le\kappa_{\max}} |\mathcal{A}_{CT}| \right], \\ [p_L, p_R] &\stackrel{\text{def}}{=} \operatorname*{argmin}_{p_L>0,\, p_R>0} \left[\max_{\kappa_{\min}\le\kappa\le\kappa_{\max}} |\mathcal{A}_{CT}| \right]. \end{aligned} \quad (83)$$

The objective function for the optimization solver DIRECT, whose minimum we seek, is thus the maximum of $|\mathcal{A}_{CT}|$ for $\kappa \in [\kappa_{\min}, \kappa_{\max}]$. To speed up the optimization process, the following modification is adopted in our code. Instead of solving for the eigenvalues of the corresponding companion matrix of the polynomial system for each κ, this matrix problem is only solved for $\kappa = h$ (which corresponds to the smoothest non-constant mode) and then homotopy continuation is applied to determine the roots for the other values of κ. Since the number of roots are different between the cases with $\kappa = 0$ and $\kappa \neq 0$, we treat $\kappa = 0$ separately in the homotopy continuation solver. Both cases have been implemented using PHCPack [25].

Once the values of p_m are found using the optimization procedure, the stability of the CHAMP time-stepping scheme can be confirmed by applying the argument principle to the complex function $G(1/A)$ for the unit circle $|A| = 1$. Let

$$\mathcal{P} = \frac{1}{2\pi i} \int_0^{2\pi} \frac{G'(e^{-i\phi})}{G(e^{-i\phi})}\, d\phi. \quad (84)$$

We note that there are no branch cuts of $G(1/A)$ for $|A| < 1$, and that there is only one simple pole of $G(1/A)$ at the origin. Therefore $\mathcal{P} = N - 1$, where N is the number roots of $G(A)$ with $|A| > 1$ [26]. The calculation of $\mathcal{P}$ provides an independent check of the stability of the CHAMP time-stepping algorithm for given values of p_m. If $\mathcal{P} = -1$, then we conclude that there no unstable roots of $G(A)$ and thus the algorithm is stable. If this check indicates that unstable roots exist for the values of p_m, then more sub-iterations can be taken. Normally each additional sub-iteration increases the stable range of parameters (e.g. range of λ_d) quite dramatically and thus zero or one iteration will likely suffice for almost all problems of interest.

[7] The assumption, $|\widetilde{\zeta}_m| \ll 1$, is a valid assumption when $\lambda_d \gg 1$ (typically true when time-stepping with an implicit solver such as BDF), $\beta = O(1)$ and $|A| = O(1)$. If $|A|$ is close to zero, then $|\widetilde{\zeta}_m|$ may not be small, but this case is not important since it does not correspond to instability.

CHAMP time-stepping: $\beta = 1$, $\lambda_d = 10^6$			
θ	p_L	p_R	$\mathcal{A}^*_{CT}$
1.00e-02	4.13e-02	6.19e-03	2.73e-01
4.64e-02	5.36e-02	3.77e-03	3.97e-01
2.15e-01	3.65e-02	4.86e-03	6.88e-01
1.00e+00	6.27e-03	2.69e-02	8.86e-01
4.64e+00	4.86e-03	3.65e-02	6.88e-01
2.15e+01	3.77e-03	5.36e-02	3.97e-01
1.00e+02	6.19e-03	4.13e-02	2.73e-01

CHAMP time-stepping: $\beta = 1$, $\theta = 1$			
λ_d	p_L	p_R	$\mathcal{A}^*_{CT}$
2.00e+07	2.58e-03	1.24e-02	1.00e+00
1.00e+07	3.35e-03	1.62e-02	9.68e-01
5.00e+06	4.49e-03	1.66e-02	9.56e-01
2.50e+06	2.10e-02	4.94e-03	9.25e-01
1.25e+06	5.98e-03	2.58e-02	8.99e-01
6.25e+05	3.28e-02	6.73e-03	8.58e-01
3.12e+05	3.58e-02	8.78e-03	8.32e-01

CHAMP time-stepping: $\theta = 1$, $\lambda_d = 10^6$			
β	p_L	p_R	$\mathcal{A}^*_{CT}$
1.00e-02	2.11e-02	4.81e-03	9.26e-01
4.64e-02	2.19e-02	5.01e-03	9.20e-01
2.15e-01	2.38e-02	5.42e-03	9.08e-01
1.00e+00	6.27e-03	2.69e-02	8.86e-01
4.64e+00	8.66e-03	3.38e-02	8.42e-01
2.15e+01	1.30e-02	4.39e-02	7.86e-01
1.00e+02	6.43e-02	1.37e-02	7.18e-01

Table 2: Optimized amplification factor, $\mathcal{A}^*_{CT}$, for the uniterated CHAMP time-stepping scheme and corresponding values for p_m for various choices of the dimensionless parameters $\theta = \mathcal{K}_L/\mathcal{K}_R$, $\beta = \mathcal{D}_L/\mathcal{D}_R$, and $\lambda_d = (\Delta t\, \mathcal{D}_L)/h^2$.

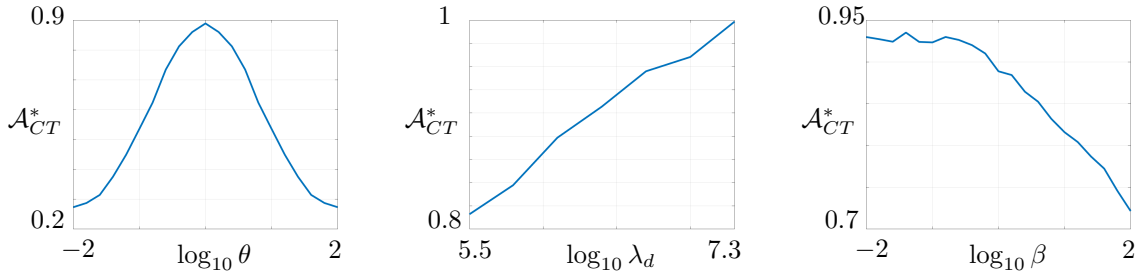

Figure 6: Magnitude of the uniterated CHAMP time-stepping amplification factor $\mathcal{A}^*_{CT}$ (of possible unstable modes) with approximately optimal p_L and p_R. Left: $\mathcal{A}^*_{CT}$ as a function of θ for $\lambda_d = 10^6$ and $\beta = 1$. Middle: $\mathcal{A}^*_{CT}$ as a function of λ_d for $\beta = 1$ and $\theta = 1$. Right: $\mathcal{A}^*_{CT}$ as a function of β for $\lambda_d = 10^6$ and $\theta = 1$. Note that $\theta = \mathcal{K}_L/\mathcal{K}_r$, $\beta = \mathcal{D}_l/\mathcal{D}_R$ and $\lambda_d = (\Delta t\, \mathcal{D}_L)/h^2$.

Values for $\mathcal{A}^*_{CT}$ and the corresponding values for the parameters p_L and p_R obtained using the optimization procedure are given in Table 2 for a number of relevant combinations of parameters θ, β and λ_d. In addition, Figure 6 shows the behavior of $\mathcal{A}^*_{CT}$ for a number of different parameter combinations[8]. The left plot shows the time-stepping amplification factor $\mathcal{A}^*_{CT}$ with θ varying between 10^{-2} and 10^2 and with $\lambda_d = 10^6$ and $\beta = 1$. As in the iteration case (see Figure 4), the amplification factor peaks at $\theta = 1$, and then decreases as the ratio of the thermal conductivities becomes large or small. The middle plot shows the behavior of $\mathcal{A}^*_{CT}$ as λ_d varies with θ and β held fixed. As before, we observe that $\mathcal{A}^*_{CT}$ increases as λ_d

[8]Values of $\mathcal{A}^*_{CT}$ in Table 2 and Figure 6 correspond to the roots of $\tilde{G}(A)$ for which ζ_m has a non-zero real part. These are the roots of interest following the result in Lemma 1. We note, however, that there may be roots of $\tilde{G}(A)$ for which ζ_m is pure imaginary and for which $|A| > \mathcal{A}^*_{CT}$, but these roots do not correspond to modes that can become unstable, and thus they are omitted.

Δy	Δt	un-iterated CHAMP with EXT2				un-iterated CHAMP with EXT3			
		Domain 0		Domain 1		Domain 0		Domain 1	
		$e_{T,0}$	ratio	$e_{T,1}$	ratio	$e_{T,0}$	ratio	$e_{T,1}$	ratio
1/160	1/160	2.02e-3	-	1.81e-3	-	5.52e-4	-	5.53e-4	-
1/320	1/320	7.13e-4	2.83	6.58e-4	2.75	1.28e-4	4.31	1.28e-4	4.31
1/640	1/640	2.65e-4	2.69	2.51e-4	2.62	3.14e-5	4.08	3.14e-5	4.08
1/1280	1/1280	1.03e-4	2.57	9.79e-5	2.56	7.77e-6	4.04	7.77e-6	4.04
rate		1.4		1.4		2.0		2.0	

Table 3: Adjacent squares with $\theta = 1$, $\beta = 1$: maximum errors and estimated convergence rates with the un-iterated CHAMP scheme with second/third order time extrapolation. The material parameters are $\mathcal{D}_1 = 1$, $\mathcal{D}_2 = 1$, $\mathcal{K}_1 = 1$ and $\mathcal{K}_2 = 1$, giving $\theta = 1$ and $\beta = 1$.

increases. We note that $\mathcal{A}^*_{CT} = 1$ for $\log_{10} \lambda_d \approx 7.3$ which is the stability limit of the un-iterated CHAMP scheme (for $\theta = \beta = 1$). Sub-time-step iterations of the CHAMP interface conditions are required for stability of the time-stepping scheme if λ_d is larger than this limiting value. Finally, the plot on the right of Figure 6 shows the behavior of $\mathcal{A}^*_{CT}$ as β varies. Here we see a similar behavior to that of the CHAMP iteration case with $\mathcal{A}^*_{CT}$ decreasing as β increases.

We remark that the stability of the CHAMP time-stepping scheme can also be considered for the case of Crank-Nicolson (CN) time integration. The analysis proceeds as before and the amplification factor still satisfies (80), but with the definitions of $\widetilde{\zeta}_m$ changes to

$$\widetilde{\zeta}_L = \sqrt{\frac{2}{\lambda_d}\frac{A-1}{A+1} + \kappa^2}, \qquad \widetilde{\zeta}_R = \sqrt{\frac{2\beta}{\lambda_d}\frac{A-1}{A+1} + \kappa^2}.$$

This change, however, creates a difficulty for the optimization problem since when $A \approx -1$, the values of $|\widetilde{\zeta}_m|$ are not small regardless of the size of λ_d and λ_d/β. This difference between CN and BDF2 is tied to the fact that BDF2 has stiff decay while CN does not. An implication of this for the optimization approach we have adopted is that the Taylor polynomial approximation used to obtain $\tilde{G}(A)$ is no longer appropriate. In addition, we have observed that for the CN case there are solutions to $G(A) = 0$ with $A \approx -1$ which correspond to nearly undamped spurious oscillations in time. This mode is often found to be the first to become unstable as the problem becomes more difficult, for example as λ_d becomes large. However, we recall the CHAMP iteration converges rapidly, and thus the time-stepping instability for CN could be suppressed by increasing the number of sub-time-step iterations.

4.2. Numerical confirmation of the accuracy of the un-iterated CHAMP time-stepping scheme

In Appendix A the accuracy of the un-iterated CHAMP time-stepping scheme is analyzed for a one-dimensional CHT problem. The analysis shows that, in terms of accuracy, the CHAMP scheme is a second-order accurate approximation to the related scheme that imposes the original interface jump conditions on the tempertaaure and heat-flux. L_2-norm energy arguments then establish the accuracy of the solution. The analysis indicates why the initial guess at each time-step requires third-order accurate extrapolation in time in equation (67), and also why the Taylor expansion leading to the CHAMP Neumann operator, $\mathbf{N}_{\theta,\beta,h}$, is truncated at $\mathcal{O}(h^2)$ in equation (48), and why the CHAMP Dirichlet operator, $\mathbf{D}_{\theta,\beta,h}$, is truncated at $\mathcal{O}(h^3)$ in equation (44). The reason has to do with the fact that the parameter $\mathbf{S}_L$ generally scales as h^{-p} for $p \in [.5, 1]$ and thus $\mathbf{S}_L$ increases in size as h decreases. The details of the analysis are given in Appendix A. Here we present some numerical results to confirm the results of the theory, in particular that third-order extrapolation in time is generally required.

Table 3 presents grid convergence results from the un-iterated CHAMP scheme using either a second-order (EXT2) or third-order (EXT3) extrapolation in time as the initial guess for the interface conditions at each time-step. The grid setup consists of two adjacent squares as described in Section 6.1. The exact solution is defined through a manufactured solution, also described in Section 6.1, using the trigonometric function in (101) with $f_x = 0$, $g_x = 0$, $f_y = 3.1$, $g_y = 0$, $f_t = 1.1$ and $g_t = 0$. The results in Table 3 for the maximum-norm errors provide strong evidence that the un-iterated CHAMP scheme with EXT3 is

Δy	Δt	CHAMP with EXT2 and 10 iterations				CHAMP with EXT3 and 10 iterations			
		Domain 0		Domain 1		Domain 0		Domain 1	
		$e_{T,0}$	ratio	$e_{T,1}$	ratio	$e_{T,0}$	ratio	$e_{T,1}$	ratio
1/160	1/160	5.38e-4	-	5.38e-4	-	5.38e-4	-	5.38e-4	-
1/320	1/320	1.26e-4	4.27	1.26e-4	4.27	1.26e-4	4.27	1.26e-4	4.27
1/640	1/640	3.10e-5	4.06	3.10e-5	4.06	3.10e-5	4.06	3.10e-5	4.06
1/1280	1/1280	7.73e-6	4.01	7.73e-6	4.01	7.73e-6	4.01	7.73e-6	4.01
rate		2.0		2.0		2.0		2.0	

Table 4: Adjacent squares with $\theta = 1$, $\beta = 1$: maximum errors and estimated convergence rates with the CHAMP scheme with 10 iterations per time-step and second/third order time extrapolation. The material parameters are $\mathcal{D}_1 = 1$, $\mathcal{D}_2 = 1$, $\mathcal{K}_1 = 1$ and $\mathcal{K}_2 = 1$, giving $\theta = 1$ and $\beta = 1$.

second-order accurate while EXT2 is not. Additional numerical experiments in Section 6 provide further confirmation that the un-iterated scheme with EXT3 is second-order accurate. For completeness, Table 4 gives the corresponding results when 10 sub-iterations are used at each time-step. In this case both EXT2 and EXT3 result in second-order accurate convergence since the order of the initial extrapolation does not matter if the equations have been iterated to a small enough tolerance.

5. Solution approach and discretization on composite grids

Having developed and analyzed the CHAMP iteration and time-stepping scheme for the model problem in (6)–(11), we return to the more general two-dimensional CHT problem defined in (1)–(5) and depicted in Figure 1. The discretization of the CHT problem uses composite overset grids as discussed, for example, in [3, 18, 27], and illustrated in the right plot of Figure 1. The CHT problem is defined for a domain Ω which is the union of a set of non-overlapping subdomains $\{\Omega_m\}$. The heat equation in (1) for each subdomain Ω_m with interface conditions in (3) and (4), and possibly with boundary conditions in (2), is discretized on a composite grid. The composite grid for Ω_m consists of a collection of component grids $\mathcal{G}_g$, $g \in [g_1, g_2]$, that cover Ω_m and overlap where they meet[9]. Each component grid is logically rectangular and defined by a smooth mapping, $\mathbf{x} = \mathbf{G}_g(\mathbf{r})$, from computational space $\mathbf{r} = (r_1, r_2)$, e.g. the unit-square in two dimensions, to physical space $\mathbf{x} = (x, y) = (x_1, x_2)$. Interpolation formulas are used to communicate the solution at the overlap between component grids (see [18]). Figure 7 illustrates a simple composite grid consisting of an annular grid in green, a Cartesian grid in blue, and interpolation points for each component grid marked with solid circles. We note that the composite grid for each subdomain conforms to the interfaces and boundaries so that the interface conditions and boundary conditions can be simply approximated in a smooth and accurate manner. Finally, we let $\mathcal{G} = \{\mathcal{G}_g\}$, $g \in [1, \mathcal{N}]$, denote the multi-domain composite grid that consist of the full set of all component grids covering the entire problem domain Ω.

5.1. Discretization of the governing equations on overlapping grids

In preparation for a discretization using overlapping grids, the governing equations and the boundary and interface conditions for a subdomain Ω_m are transformed from physical space coordinates to computational space coordinates for a given mapping $\mathbf{x} = \mathbf{G}_g(\mathbf{r})$. This transformation is accomplished using the chain rule, e.g.

$$\frac{\partial T_m}{\partial x_i} = \frac{\partial r_j}{\partial x_i} \frac{\partial T_m}{\partial r_j}, \tag{85}$$

where the summation convection is assumed for repeated indices. The metrics, $\partial r_j / \partial x_i$, $i, j = 1$ or 2, for the mapping $\mathbf{x} = \mathbf{G}_g(\mathbf{r})$ depend on the component grid number g, but this dependency is suppressed when

[9]The overlap for a composite grid is introduced for flexibility in handling complex, and possibly moving, geometries and should not be confused with the domain overlap as in OS.

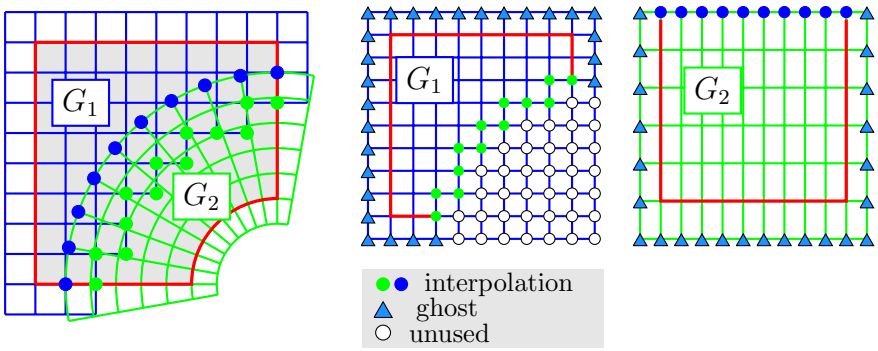

Figure 7: Left: an overlapping grid consisting of two structured curvilinear component grids, $\mathbf{x} = G_1(\mathbf{r})$ and $\mathbf{x} = G_2(\mathbf{r})$. Middle and right: component grids for the square and annular grids in the unit square parameter space $\mathbf{r}$. Grid points are classified as discretization points, interpolation points or unused points. Ghost points are used to apply boundary conditions.

possible for notational convenience. Since the material properties are constant on each component grid, the heat equation transforms to

$$\partial_t T_m = \frac{\mathcal{K}_m}{\rho_m C_m} \Delta T_m + f(\mathbf{x}(\mathbf{r}), t), \tag{86}$$

where

$$\Delta = A_{ij} \frac{\partial^2}{\partial r_i \partial r_j} + c_i \frac{\partial}{\partial r_i}, \qquad A_{ij} \stackrel{\text{def}}{=} \frac{\partial r_i}{\partial x_k} \frac{\partial r_j}{\partial x_k}, \qquad c_i \stackrel{\text{def}}{=} \frac{\partial}{\partial x_k} \frac{\partial r_i}{\partial x_k}. \tag{87}$$

Alternatively, the Laplacian operator can be approximated in a discrete self-adjoint form, if desired, see [28]. Note that the unit normal along a coordinate curve $r_i(x, y) = \text{constant}$ is

$$\mathbf{n}_i = \frac{\nabla_{\mathbf{x}} r_i}{\|\nabla_{\mathbf{x}} r_i\|}, \qquad \nabla_{\mathbf{x}} r_i = \begin{bmatrix} \frac{\partial r_i}{\partial x} \\ \frac{\partial r_i}{\partial y} \end{bmatrix}, \tag{88}$$

so that the normal derivative is given by

$$\mathbf{n}_i \cdot \nabla_{\mathbf{x}} T_m = \frac{1}{\|\nabla_{\mathbf{x}} r_i\|} \frac{\partial r_i}{\partial x_k} \frac{\partial r_j}{\partial x_k} \frac{\partial T_m}{\partial r_j} \stackrel{\text{def}}{=} B_{ij} \frac{\partial T_m}{\partial r_j}. \tag{89}$$

For an external boundary along a curve $r_1(x, y) = \text{constant}$, for example, the boundary condition in (2) becomes

$$a\, T_m + b\, \mathbf{n}_1 \cdot \nabla_{\mathbf{x}} T_m = g_m(r_2, t), \qquad r_1 = \text{constant}, \tag{90}$$

where the normal derivative of T_m is defined in (88) and (89). We note that if the coordinates in the computational domain are orthogonal, i.e. if $\mathbf{n}_1 \cdot \mathbf{n}_2 = 0$, then the matrix B_{ij} in (89) becomes diagonal and the formula for the normal derivative simplifies.

The interface conditions in (3) and (4) involve the continuity of temperature and heat flux at the interface separating two subdomains. Let $m = L$ denote the "left" subdomain and $m = R$ denote the "right" subdomain, and suppose the interface along a common boundary of the subdomains is given by $r_1(x, y) = \text{constant}$. For this configuration, the interface conditions become

$$T_L = T_R, \qquad \mathcal{K}_L \big(\mathbf{n}_1 \cdot \nabla_{\mathbf{x}}\big)\big|_{g_L} T_L = \mathcal{K}_R \big(\mathbf{n}_1 \cdot \nabla_{\mathbf{x}}\big)\big|_{g_R} T_R, \qquad r_1 = \text{constant}. \tag{91}$$

Here, we note that the normal derivative operators involve metrics of a mapping, $\mathbf{x} = \mathbf{G}_g(\mathbf{r})$, for component grids $g = g_L$ or g_R in each subdomain.

The mapped equations in (86) are discretized on a uniform grid with mesh spacings Δr_1 and Δr_2 in the computational domain. Spatial derivatives of T_m are approximated using second-order accurate central differences. The metrics $\partial r_i / \partial x_j$ are assumed known from the mapping while derivatives of the metrics, such

as those found in c_i in (87) are determined with finite difference. Ghost points are introduced to facilitate a second-order accurate approximation of the boundary conditions in (90). The interface conditions in (91) are manipulated into the CHAMP conditions, as we describe next, and then discretized using second-order accurate approximations.

5.2. The CHAMP conditions on a curvilinear grid

In this section the form of the CHAMP Dirichlet (47) and Neumann (49) interface operators for curvilinear grids are derived. To simplify the presentation, we assume that the coordinates of the mapped domains on each side of the interface are orthogonal. Further, we consider an interface given by $r_1(x,y) = 0$ for each domain. With these assumptions, continuity of heat flux at the interface from the mapped interface conditions in (91) becomes

$$\mathcal{K}_L\, B^L_{11}\, \frac{\partial T_L}{\partial r_1} = \mathcal{K}_R\, B^R_{11}\, \frac{\partial T_R}{\partial r_1}, \qquad \text{for } r_1 = 0, \tag{92}$$

where B^L_{11} and B^R_{11} are defined in (89) for grids g_L and g_R, respectively. The compatibility interface condition $\left[\mathcal{D}\Delta T\right]_{\mathcal{I}} = 0$, derived from the continuity of temperature in (91) and the mapped equations in (86), implies

$$\mathcal{D}_L \Delta T_L = \mathcal{D}_R \left(A^R_{11} \frac{\partial^2 T_R}{\partial r_1^2} + A^R_{22} \frac{\partial^2 T_R}{\partial r_2^2} + c^R_1 \frac{\partial T_R}{\partial r_1} + c^R_2 \frac{\partial T_R}{\partial r_2} \right) T_R, \qquad \text{for } r_1 = 0, \tag{93}$$

where the Δ operator has been written out explicitly for the right domain in terms of A^R_{ij} and c^R_i defined in (87) for grid g_R. As in the Cartesian case discussed previously in Section 3.3, the CHAMP conditions for the left domain use a Taylor expansion of the solution on the right domain at an overlap distance of h_R,

$$T_R(h_R, r_2) = T_R(0, r_2) + h_R \frac{\partial T_R}{\partial r_1}(0, r_2) + \frac{h_R^2}{2} \frac{\partial^2 T_R}{\partial r_1^2}(0, r_2) + \mathcal{O}(h_R^3). \tag{94}$$

Equations (92) and (93) are used to replace the "normal derivatives" $\partial_{r_1} T_R$ and $\partial^2_{r_1} T_R$ in (94) in terms of "tangential" derivatives in the r_2-direction and normal derivatives of T_L. After dropping $\mathcal{O}(h_R^3)$ terms and higher in (94) we arrive at the CHAMP Dirichlet-like condition for the left domain about the interface $r_1 = 0$,

$$\mathbf{D}_L\left[T_L(0, r_2)\right] \stackrel{\text{def}}{=} T_L(0, r_2) + \tilde{\theta}\, h_R\, \partial_{r_1} T_L(0, r_2) + \frac{h_R^2}{2} \mathcal{L}_L T_L(0, r_2) = T_R(h_R, r_2), \tag{95}$$

where

$$\mathcal{L}_L \stackrel{\text{def}}{=} \frac{1}{A^R_{11}} \left[\beta\, \Delta \; - A^R_{22} \partial^2_{r_2} - \tilde{\theta}\, c^R_1\, \partial_{r_1} - c^R_2 \partial_{r_2} \right], \qquad \tilde{\theta} \stackrel{\text{def}}{=} \frac{\mathcal{K}_L}{\mathcal{K}_R} \frac{B^L_{11}}{B^R_{11}} = \theta\, \frac{B^L_{11}}{B^R_{11}}, \qquad \beta = \frac{\mathcal{D}_L}{\mathcal{D}_R}.$$

The CHAMP Dirichlet-like condition in (95) for a curvilinear grid corresponds to (47) for a Cartesian grid. Similarly, a Taylor expansion for $\partial_{r_1} T_R(h_R, r_2)$ about $r_1 = 0$ and the heat flux condition in (92) leads to the CHAMP generalized-Neumann condition,

$$\mathbf{N}_L\left[T_L(0, r_2)\right] \stackrel{\text{def}}{=} \tilde{\theta}\, \partial_{r_1} T(0, r_2) + h_R\, \mathcal{L}_L T_L(0, r_2) = \partial_{r_1} T_R(h_R, r_2), \tag{96}$$

which is the curvilinear version of the CHAMP Neumann-like condition in (49). Summing the Dirichlet and Neumann conditions in (95) and (96), respectively, with weighting S_L, gives the extension of the CHAMP interface condition for the left domain in (50) for a curvilinear grid. The extension of the CHAMP interface condition for the right domain in (51) can be derived following an analogous procedure.

For the case of curvilinear grids, the determination of optimal weights is complicated by the fact that the mapped heat equation in (86) and the CHAMP conditions in (95) and (96) have variable coefficients and terms involving lower-order derivatives. These complications are avoided by considering a local analysis with frozen coefficients and with lower-order terms dropped. Values for $S_L = p_L$ and $S_R = p_R$ are determined

following a similar procedure as that described in Section 4 for a polynomial system involving $\tilde{G}(A)$ defined in (82), but with the polynomial equations for $\widetilde{\zeta}_L$ and $\widetilde{\zeta}_R$ replaced by

$$\left(\widetilde{\zeta}_L\right)^2 = \frac{1}{\tilde{\lambda}_d}\,\frac{3A^2-4A+1}{2A^2} + \tilde{\kappa}^2, \qquad \left(\widetilde{\zeta}_R\right)^2 = \gamma\left(\frac{\beta}{\tilde{\lambda}_d}\,\frac{3A^2-4A+1}{2A^2} + \tilde{\kappa}^2\right), \tag{97}$$

where

$$\tilde{\lambda}_d \stackrel{\text{def}}{=} A_{11}^L\,\frac{\mathcal{D}_L\Delta t}{h_L^2}, \qquad \tilde{\kappa} \stackrel{\text{def}}{=} k h_L\sqrt{\frac{A_{22}^L}{A_{11}^L}}, \qquad \gamma \stackrel{\text{def}}{=} \frac{h_R^2}{h_L^2}\,\frac{A_{11}^L}{A_{11}^R}. \tag{98}$$

This is nearly identical to the system used for optimization in Section 4 but with modified definitions for non-dimensional quantities λ_d and κ, and the inclusion of γ which represents the ratio of the normal grid spacings between the two domains. Owing to the similarities with the Cartesian grid case, the same optimization procedure is used. We note that, in general, the optimal values of p_L and p_R may vary along a given interface due to changes in the grid spacing, but in the examples considered in this paper, constant values of p_L and p_R are used at each interface as there is little variation due to the grid.

6. Numerical experiments

We now present computational results which demonstrate the convergence and accuracy properties of the CHAMP time-stepping scheme. First, the convergence rate of the CHAMP iteration is verified in Section 6.1 for two geometric configurations, one involving two adjacent squares and the other involving two concentric annular regions, each with various combinations of thermal properties. These two geometries are used in Section 6.2 to demonstrate second-order spatial accuracy of the CHAMP time-stepping scheme for the approximation of steady state solutions where the exact solutions are known. In Sections 6.3.1, the annulus-annulus geometry is used to verify second-order spatial and temporal accuracy for the un-iterated CHAMP scheme using the method of manufactured solutions for a specified solution consisting of trigonometric functions. This test case is also used to explore the time-stepping stability constraints for the un-iterated scheme, and we demonstrate that for a wide range of problems no sub-time-step iterations are needed. For some severe cases involving very large times with respect to the chosen grid size in space, we show that the un-iterated scheme can be unstable (as predicted by the analysis in Section 4.1). We also show results for the CHAMP scheme with one sub-time-step iteration and observe, as expected, that stability is regained and second-order accuracy is achieved.

Two final examples are provided that illustrate the behavior of the CHAMP scheme for problems with more complex geometric configurations involving multiple subdomains. In Section 6.3.2, numerical solutions are computed for a domain consisting of two disks in a square. As before, an exact solution is constructed for this problem using the method of manufactured solutions so that errors in the numerical solution can be assessed. In Section 6.4, an hexagonal-shaped fuel assembly with heated fuel pins is simulated and a self-convergence grid-refinement study is performed to confirm second-order accuracy. For both cases, we are able to show that the un-iterated scheme is stable and second-order accurate for problems involving more complicated domains.

Note that all test cases are solved using the CHAMP time-stepping scheme with a second-order BDF method in time, second-order accurate centered finite-differences in space, and the CHAMP conditions applied at the interface between the subdomains. In the convergence tests for the CHAMP iteration, the weights p_m are determined by solving the optimization problem described in Section 3.3.

For cases involving the un-iterated CHAMP time-stepping scheme, values for p_m are determined by approximate solutions to the optimization problem as discussed in Section 4.1 with appropriate modifications to parameters as indicated in (98). In either case, it is important to note that globally optimal values for the weights p_m are not found, in general, for three reasons. Firstly, the model problem analysis only approximately applies to the curvlinear case. Secondly, for curvilinear grids the optimal coefficients may vary along a given interface due to changes in the grid spacing, but in this manuscript constant values are used. Thirdly, only suitable local minima (i.e. resulting in a stable scheme) to the minimax problem based on (80) are found. Despite these approximations, the numerical results in this section demonstrate good agreement with the results of the model problem analyses.

6.1. Verification of the convergence rate for the CHAMP iteration

We begin by presenting computational results to confirm the analysis of the convergence rate for the CHAMP iteration discussed in Section 3.3. As a first case, we consider a domain consisting of two adjacent squares, $\Omega = \Omega_1 \cup \Omega_2$, where $\Omega_1 = [x_a, x_b] \times [y_a, y_I]$ and $\Omega_2 = [x_a, x_b] \times [y_I, y_b]$. Here, the bottom (left) domain is denoted by $L = 1$ and the top (right) domain by $R = 2$. Dirichlet boundary conditions with $T_1 = T_a = 0$ and $T_2 = T_b = 0$ are applied at $y = y_a$ and $y = y_b$, respectively, and periodic boundary conditions are applied at $x = x_a$ and $x = x_b$. A computational grid $\mathcal{G}$ with component grids $\mathcal{G}_1$ and $\mathcal{G}_2$ for the subdomains Ω_1 and Ω_2, respectively, are defined using Cartesian grids with spacings Δx and Δy in the x and y-directions respectively. (No mappings are needed for this simple geometry.) For this problem, we take $x_a = 0$, $x_b = 1$, $y_a = -1$, $y_I = 0$ and $y_b = 1$, and grid spacings $\Delta x = \Delta y = 10^{-3}$. The computational setup is illustrated on the left in Figure 8 and we note that the grid has been coarsened for presentation purposes.

The convergence rate of the CHAMP iteration is determined by taking one time-step of the partitioned CHT solver with $\Delta t = 1$, and using a sufficient number of sub-time-step iterations until convergence of the iteration is achieved. The initial state of the temperatures T_1 and T_2 for the subdomains Ω_1 and Ω_2 are taken from the function

$$T(x, y, t) = \left(\sum_{k=0}^{10} \cos\left(\pi k (x - g_x)\right) \cos\left(\pi k (y - g_y)\right) \right) \cos\left(f_t (t - g_t)\right), \tag{99}$$

evaluated at $t = 0$ and for $\mathbf{x} = (x, y)$ in each subdomain. Here, we use $g_x = 0.5$, $g_y = 0$, $f_t = 0.1$, $g_t = 0$. A third-order extrapolation in time is used to obtain an initial guess for the CHAMP interface conditions (see Step 6 in Algorithm 1) and this extrapolation uses temperatures obtained from (99) at $t = -\Delta t$ and $t = -2\Delta t$ (see (67) with $n = 0$).

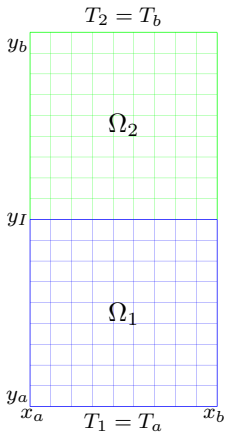

$\frac{\Delta t \mathcal{D}_1}{\Delta y^2} = \lambda_d$	$\frac{\mathcal{K}_1}{\mathcal{K}_2} = \theta$	$\frac{\mathcal{D}_1}{\mathcal{D}_2} = \beta$	$\mathcal{A}^*_{CI}$	$\mathcal{A}_{\text{comp}}$
10^6	1	1	0.36	0.35
10^6	10	1	0.069	0.062
10^6	1	0.1	0.37	0.31
10^6	0.5	0.2	0.25	0.21

Figure 8: Left: computational domain and grid for the square-square test case. Right: A comparison of the CHAMP iteration convergence rate for the square-square test for a variety of relevant physical and computational parameters. Good agreement is found between the theoretical convergence rate $\mathcal{A}^*_{CI}$, and the rate estimated from computations, $\mathcal{A}_{\text{comp}}$.

Figure 8 presents computed convergence rates for the case $\mathcal{D}_1 = \mathcal{K}_1 = 1$, and for a range of values for $\mathcal{D}_2$ and $\mathcal{K}_2$ as specified by the dimensionless parameters θ and β. The residual of the interface conditions at the j^{th} iteration is defined by

$$R^{(j)} = \max_{\mathbf{x_i} \in \mathcal{I}_h} \left\{ \left| T^{(j)}_{1,\mathbf{i}} - T^{(j)}_{2,\mathbf{i}} \right|, \left| \mathcal{K}_1 D_n T^{(j)}_{1,\mathbf{i}} - \mathcal{K}_2 D_n T^{(j)}_{2,\mathbf{i}} \right| \right\},$$

where D_n is a second-order accurate central divided-difference operator in the normal direction and the maximum is taken over all grid points, $\mathbf{x_i} = (x_i, y_j)$, on the discrete interface denoted by $\mathcal{I}_h$. The convergence rate, $\mathcal{A}_{\text{comp}}$, is computed from the decrease in the residual of the interface equations over N iterations using

$$\mathcal{A}_{\text{comp}} = \left(\frac{R^{(N)}}{R^{(1)}} \right)^{1/(N-1)},$$

where N is determined from the convergence condition

$$\left|R^{(N)} - R^{(N-1)}\right| < 10^{-10}. \tag{100}$$

The table on the right of Figure 8 compares the computed convergence rate and the theoretical value $\mathcal{A}^*_{CI}$ obtained for the model problem discussed in Section 3.3. We observe that the computed convergence rates for the CHAMP iteration are slightly smaller than, but very close to, the theoretical value. We note also that the initial state for the temperature given by (99) involves a range of wave numbers, including small wave numbers for which the convergence rate of the iteration is slowest (see Figure 5). This is done to give a good estimate of a "worst case" value for $\mathcal{A}_{\text{comp}}$.

As a second test of the CHAMP iteration, we consider a CHT problem involving the two concentric annular subdomains shown in Figure 9. Each subdomain is discretized using curvilinear grids, and we perform a similar set of calculations as was done for the previous square-square geometry. The inner subdomain Ω_1 has radial bounds $[r_a, r_I]$ and the outer subdomain Ω_2 has radial bounds $[r_I, r_b]$, where $r_a = 0.5$, $r_I = 1$ and $r_b = 1.5$. A computational grid $\mathcal{G}$ is defined for Ω with computational space (unit square) grid spacings of Δr_1 and Δr_2 corresponding to the radial and circumferential directions, respectively, where $\Delta r_1 = \Delta r_2 = 2{\times}10^{-3}$. The initial state of the temperature in each subdomain is determined from the function given in (99), and one time-step is taken as before, but with $\Delta t = 0.25$.

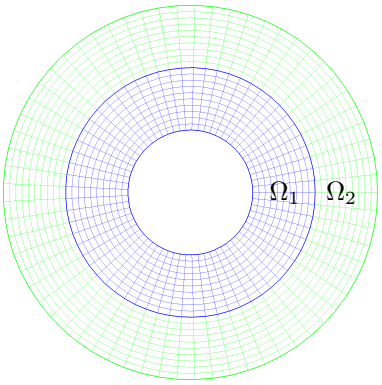

Champ iteration convergence rates				
$A^L_{11}\frac{\mathcal{D}_1\Delta t}{\Delta r_1^2} = \tilde{\lambda}_d$	$\frac{\mathcal{K}_1}{\mathcal{K}_2}\frac{B^L_{11}}{B^R_{11}} = \tilde{\theta}$	$\frac{\mathcal{D}_1}{\mathcal{D}_2} = \beta$	$\mathcal{A}^*_{CI}$	$\mathcal{A}_{\text{comp}}$
10^6	1	1	0.36	0.26
10^6	10	1	0.069	0.051
10^6	1	0.1	0.37	0.32
10^6	0.5	0.2	0.25	0.23

Figure 9: Left: grid for the annulus-annulus test case (coarsened). Right: Comparison of the CHAMP iteration convergence rate for a variety of relevant physical and computational parameters. Reasonably good agreement is shown between the theoretical rate $\mathcal{A}^*_{CI}$ (derived for the rectangular-domain model problem) and the computed rate $\mathcal{A}_{\text{comp}}$.

The table in Figure 9 compares the computed convergence rate, $\mathcal{A}_{\text{comp}}$, of the CHAMP iteration for the annulus-annulus problem to the theoretical rate, $\mathcal{A}^*_{CI}$. The latter convergence rate is determined following the extension to curvilinear grids discussed in Section 5.2. As before, we set $\mathcal{D}_1 = \mathcal{K}_1 = 1$ and vary $\mathcal{D}_2$ and $\mathcal{K}_2$. The results in the table indicate that $\mathcal{A}^*_{CI}$ provides a very good approximation to the computed convergence rates. This is despite a number of simplifying assumptions used in the analysis (e.g. using infinite domains and spatially exact operators). We note that the convergence rate at each iteration, $\mathcal{A}^{(j)} = R^{(j)}/R^{(j-1)}$, can vary considerably with the iteration step j, with $\mathcal{A}^{(j)}$ tending to be smaller at smaller values of j before increasing towards the reported value of $\mathcal{A}_{comp}$. We attribute this behavior to the fact that, as seen from Figure 5, modes with larger wave number tend to converge much faster than those with smaller wave numbers and thus the ultimate convergence rate is dominated by the modes with lower wave number.

6.2. Verification of the spatial accuracy for two steady state problems

In this section, the spatial accuracy of the un-iterated CHAMP scheme is examined by computing steady state solutions and comparing them to exact solutions [3]. We first consider a steady CHT problem with the square-square geometry illustrated in Figure 8. As before, periodic boundary conditions are applied in the x-direction, and constant temperatures $T = T_a$ and $T = T_b$ are specified at $y = y_a$ and $y = y_b$, respectively. The steady state solution is computed by time-stepping the solution from a constant initial state given by

$$T_1(x, y, 0) = T_2(x, y, 0) = \frac{1}{2}\left(T_a + T_b\right),$$

for T_1 and T_2 in the two subdomains. The exact steady solution for this problem depends only on the vertical coordinate y and is given by

$$\bar{T}_1(y) = T_a + \frac{y - y_a}{y_I - y_a}\,(T_I - T_a)\,, \qquad \bar{T}_2(y) = T_I + \frac{y - y_I}{y_b - y_I}\,(T_b - T_I)\,,$$

where the temperature at the interface is given by

$$T_I = \frac{\mathcal{K}_1 T_b + \mathcal{K}_2 T_a}{\mathcal{K}_1 + \mathcal{K}_2}.$$

Simulations are performed using the square-square configuration defined by $x_a = -1$, $x_b = 1$, $y_a = -1$, $y_I = 0$ and $y_b = 1$, and with grid spacings $\Delta x = \Delta y = 0.025$. The temperatures at the boundaries are taken to be $T_a = 5$ and $T_b = 1$, and the material parameters are $\mathcal{D}_1 = 1$, $\mathcal{D}_2 = 0.5$, $\mathcal{K}_1 = 0.1$ and $\mathcal{K}_2 = 0.2$. The un-iterated CHAMP time-stepping scheme is run with $\Delta t = 1$ to a final time $t_{\text{final}} = 100$, which is sufficient for the solution to settle to steady state with a residual of the interface conditions equal to 1.78×10^{-13} approximately. Since the approximation of the governing equations and interface conditions is second-order accurate and since the exact solution is linear in each domain, we expect the numerical solution to be exact to within round-off errors. We find that the maximum error in the computed solution is 1.51×10^{-13}, which is in agreement with our expectation for double-precision arithmetic.

We next consider the CHT problem on the annulus-annulus geometry as illustrated in Figure 9. The temperature at the inner boundary is taken to be $T_1 = T_a$, while the temperature at the outer boundary is $T_2 = T_b$. The initial temperature in the two subdomains is given by the average value

$$T_1(x, y, 0) = T_2(x, y, 0) = \frac{1}{2}\,(T_a + T_b)\,.$$

The steady state solution depends only on the radial distance r and is given by

$$\bar{T}_1(r) = T_a + \frac{\ln(r/r_a)}{\ln(r_I/r_a)}\,(T_I - T_a)\,, \qquad \bar{T}_2(r) = T_I + \frac{\ln(r/r_I)}{\ln(r_b/r_I)}\,(T_b - T_I)\,,$$

where

$$T_I = \frac{\mathcal{K}_1 \ln(r_I/r_a)\, T_b + \mathcal{K}_2 \ln(r_b/r_I)\, T_a}{\mathcal{K}_1 \ln(r_I/r_a) + \mathcal{K}_2 \ln(r_b/r_I)}.$$

Simulations are carried out using $r_a = 0.2$, $r_I = 0.4$ and $r_b = 0.6$. The boundary temperatures are taken as $T_a = 5$ and $T_b = 1$, and the material parameters are taken to be $\mathcal{D}_1 = 1$, $\mathcal{D}_2 = 0.5$, $\mathcal{K}_1 = 0.1$ and $\mathcal{K}_2 = 0.2$. As before, we integrate the equations to steady state at a final time $t_{\text{final}} = 100$ using the un-iterated CHAMP time-stepping algorithm with $\Delta t = 1$. The plot on the left of Figure 10 shows the exact steady state solution (solid curves) and the numerical solution (marks) for a calculation on curvilinear grids with physical-space grid spacings $h_r = .0025$ in the radial direction and $h_\phi = .0052$ in circumferential direction (along $r = r_I$). We observe excellent agreement of the two solutions. A quantitative assessment of the error in the numerical solution at steady state can be made by computing the max-norm errors in the solution for different grid resolutions. The table on the right of Figure 10 gives the results of a convergence study of this numerical error in the solution. Max-norm errors in the temperature are computed for three different grid resolutions given by h_r and h_ϕ. The values in the table show that the ratio of the errors is approximately equal to four as the grid spacings are reduced by half indicating second-order accuracy. The estimated convergence rate given in the table is computed using a least-squares fit to the logarithm of the errors versus the logarithm of the grid spacings, and this estimate also confirms second-order accuracy of the approximation. Note that temporal accuracy is not assessed in this convergence study since the numerical error is computed at steady state.

6.3. Convergence analysis using the method of manufactured solutions

In the previous section, the spatial accuracy of the CHAMP time-stepping scheme was verified for two steady state problems. In this section, the spatial and temporal accuracy of the CHAMP time-stepping scheme is investigated using the *method of manufactured solutions*, a name coined by Roache [29], but earlier

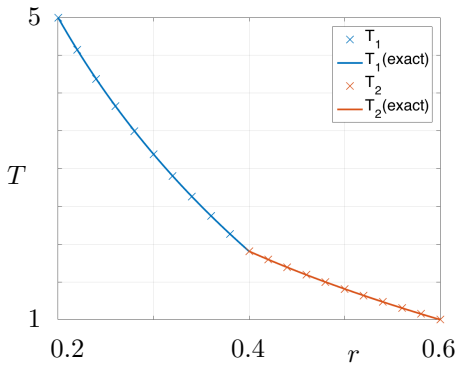

Annulus-annulus, $\theta = \frac{\mathcal{K}_1}{\mathcal{K}_2} = \frac{1}{2}$, $\beta = \frac{\mathcal{D}_1}{\mathcal{D}_2} = 2$			
h_r	h_ϕ	max error	ratio
1.0e-02	2.1e-02	1.10e-03	-
5.0e-03	1.1e-02	2.64e-04	4.17
2.5e-03	5.2e-03	6.44e-04	4.10
rate		2.03	

Figure 10: Results of a convergence study for the annulus-annulus problem using an exact steady state solution. An estimated convergence rate is determined from the max-norm errors of the temperature computed for the entire domain. The estimate indicates second-order accuracy.

referred to as *twilight zone forcing* by D. Brown [30, 31] in reference to its use in [32]. In the method of manufactured solutions, an exact solution is constructed by adding forcing terms to the governing equations (PDEs, initial conditions, boundary conditions, and interface conditions) so that the chosen function for the temperature becomes the exact solution to the forced equations. For detailed information on the construction of forcing functions for CHT problems refer to [3]. The focus here is on illustrating the behavior of the CHAMP scheme, and for this purpose we choose two problem configurations. The first problem is defined for a quarter-section of the previous annulus-annulus geometry, and it is used to demonstrate second-order accuracy in space and time, as well as to illustrate the stability limitations of the un-iterated scheme for very large time steps. For the case where the un-iterated scheme is unstable, an extended CHAMP scheme using one sub-time-step iteration is shown to regain stability, and therefore second-order accuracy under mesh refinement. The second test returns to the two-disks-in-a-square geometry illustrated in Figure 1. This test is used to demonstrate second-order accuracy of the CHAMP scheme for the case when overlapping grids are used in the discretization of the equations on the subdomains.

6.3.1. Quarter annulus-annulus geometry

Consider a quarter-section of the annulus-annulus geometry from Figure 9 with $r_a = 0.5$, $r_I = 1$ and $r_b = 1.5$, and with opening angle $\phi \in [0, \pi/2]$[10]. Dirichlet boundary conditions are imposed along the sides $\phi = 0$ and $\phi = \pi/2$, and on the inner and outer boundaries at $r = r_a$ and $r = r_b$. For this configuration, Ω_1 is the inner quarter annulus and Ω_2 is the outer quarter annulus. Appropriate forcing functions are obtained so that the exact solution is given by

$$T_e(x, y, t) = \cos(f_x(x - g_x))\, \cos(f_y(y - g_y))\, \cos(f_t(t - g_t)), \tag{101}$$

with $f_x = 2$, $g_x = 0.5$, $f_y = 2$, $g_y = 0$, $f_t = 0.013$ and $g_t = 0$. The numerical solution is computed on a sequence of grids with increasing resolution for three different combinations of thermal diffusivities and conductivities, and max-norm errors of the temperature in each subdomain are determined at a final time, $t_{\text{final}} = 40$.

In the first test, we set $\mathcal{D}_1 = \mathcal{D}_2 = 1$ and $\mathcal{K}_1 = \mathcal{K}_2 = 1$ so that $\theta = \frac{\mathcal{K}_1}{\mathcal{K}_2} = 1$ and $\beta = \frac{\mathcal{D}_1}{\mathcal{D}_2} = 1$. Table 5 reports max-norm errors for the un-iterated CHAMP scheme and the CHAMP scheme with one sub-time-step iteration as a function of the physical-space grid spacings h_r and h_ϕ. In the table, $\mathcal{E}_m$ denotes the max-norm error in the temperature for the domain Ω_m, $m = 1$ and 2, the grid spacing h_r is listed and h_ϕ is chosen as $h_\phi = 6.25\pi \times h_r$. For these computations the time-step, Δt, is chosen to scale in proportion to the grid size, and so $\tilde{\lambda}_d = \mathcal{D}_1 \Delta t / h_r^2$ increases as the grid spacings decrease. The optimization used in Section 5.2, based on the model problem analysis, indicates that the un-iterated scheme is stable for $\tilde{\lambda}_d \lesssim 10^7$. As shown

[10]The quarter section is considered for convenience to speed up the computation of all the results needed to estimate convergence rates.

Quarter annulus-annulus: $\theta = \frac{\mathcal{K}_1}{\mathcal{K}_2} = 1$ and $\beta = \frac{\mathcal{D}_1}{\mathcal{D}_2} = 1$										
h_r	Δt	$\tilde{\lambda}_d = \frac{\mathcal{D}_1 \Delta t}{h_r^2}$	un-iterated CHAMP				CHAMP with 1 iteration			
			Domain Ω_1		Domain Ω_2		Domain Ω_1		Domain Ω_2	
			$\mathcal{E}_1$	ratio	$\mathcal{E}_2$	ratio	$\mathcal{E}_1$	ratio	$\mathcal{E}_2$	ratio
1.6e-3	0.8	1.25e+6	2.61e-4	–	3.23e-4	–	2.34e-4	–	3.26e-4	–
8.0e-4	0.4	2.5e+6	6.11e-5	4.27	8.10e-5	3.98	5.85e-5	4.00	8.11e-5	4.02
4.0e-4	0.2	5.0e+6	1.50e-5	4.07	2.02e-5	4.01	1.46e-5	4.01	2.03e-5	4.00
2.0e-4	0.1	1.0e+7	unstable	–	unstable	–	3.65e-6	4.00	5.07e-6	4.00
rate			2.0		2.0		2.0		2.0	

Table 5: Quarter annulus-annulus with $\theta = 1$ and $\beta = 1$: Maximum errors and estimated convergence rates for the un-iterated CHAMP time-stepping scheme and the CHAMP scheme with one sub-time-step iteration. The inner quarter-annulus is the domain Ω_1, while the outer quarter-annulus is Ω_2. See also Fig. 11 for graphs of this data.

Quarter annulus-annulus: $\theta = \frac{\mathcal{K}_1}{\mathcal{K}_2} = 1$ and $\beta = \frac{\mathcal{D}_1}{\mathcal{D}_2} = 10^{-2}$										
h_r	Δt	$\tilde{\lambda}_d = \frac{\mathcal{D}_1 \Delta t}{h_r^2}$	un-iterated CHAMP				CHAMP with 1 iteration			
			Domain Ω_1		Domain Ω_2		Domain Ω_1		Domain Ω_2	
			$\mathcal{E}_1$	ratio	$\mathcal{E}_2$	ratio	$\mathcal{E}_1$	ratio	$\mathcal{E}_2$	ratio
1.6e-3	0.8	1.25e+6	2.08e-4	–	3.30e-4	–	2.35e-4	–	3.27e-4	–
8.0e-4	0.4	2.5e+6	6.46e-5	3.23	8.10e-5	4.07	5.90e-5	3.98	8.15e-5	4.01
4.0e-4	0.2	5.0e+6	1.51e-5	4.27	2.02e-5	4.01	1.49e-5	3.96	2.03e-5	4.01
2.0e-4	0.1	1.0e+7	unstable	–	unstable	–	3.66e-6	4.07	5.10e-6	3.98
rate			1.9		2.0		2.0		2.0	

Table 6: Quarter annulus-annulus with $\theta = 1$ and $\beta = 10^{-2}$: Maximum errors and estimated convergence rates for the un-iterated CHAMP time-stepping scheme and the CHAMP scheme with one sub-time-step iteration. The inner quarter-annulus is the domain Ω_1, while the outer quarter-annulus is Ω_2. See also Fig. 11 for graphs of this data.

Quarter annulus-annulus: $\theta = \frac{\mathcal{K}_1}{\mathcal{K}_2} = 10^{-2}$ and $\beta = \frac{\mathcal{D}_1}{\mathcal{D}_2} = 1$										
h_r	Δt	$\tilde{\lambda}_d = \frac{\mathcal{D}_1 \Delta t}{h_r^2}$	un-iterated CHAMP				CHAMP with 1 iteration			
			Domain Ω_1		Domain Ω_2		Domain Ω_1		Domain Ω_2	
			$\mathcal{E}_1$	ratio	$\mathcal{E}_2$	ratio	$\mathcal{E}_1$	ratio	$\mathcal{E}_2$	ratio
1.6e-3	0.8	1.25e+6	2.87e-4	–	3.33e-4	–	2.79e-4	–	3.33e-4	–
8.0e-4	0.4	2.5e+6	6.96e-5	4.12	8.29e-5	4.02	6.95e-5	4.01	8.30e-5	4.01
4.0e-4	0.2	5.0e+6	1.74e-5	4.00	2.07e-5	4.00	1.74e-5	3.99	2.07e-5	4.01
2.0e-4	0.1	1.0e+7	4.34e-6	4.01	5.18e-6	4.00	4.34e-6	4.01	5.18e-6	4.00
rate			2.0		2.0		2.0		2.0	

Table 7: Quarter annulus-annulus with $\theta = 10^{-2}$ and $\beta = 1$: Maximum errors and estimated convergence rates for the un-iterated CHAMP time-stepping scheme and the CHAMP scheme with one sub-time-step iteration. The inner quarter-annulus is the domain Ω_1, while the outer quarter-annulus is Ω_2. See also Fig. 11 for graphs of this data.

in Table 5, the un-iterated CHAMP scheme converges at close to second-order accuracy for all but the finest grid where the scheme becomes unstable. For this finest grid, $\tilde{\lambda}_d \approx 5 \times 10^6$ which is very close to the stability limit predicted by the analysis. We observe that the CHAMP time-stepping scheme with one sub-time-step is second-order accurate and stable for all grids tested, including the finest grid. Note that the values for Δt chosen in Table 5 are, for many purposes, quite large so that this convergence study is a severe test of the un-iterated scheme. In practice, for accuracy reasons, the size of the time-step is often chosen proportional to the grid spacing (e.g. the time-step based on the advection terms in the Navier-Stokes equations for a full CHT problem). If $\Delta t \approx h_r$ and $\mathcal{D}_1 \approx 1$, for example, then the stability limit $\tilde{\lambda}_d \approx 10^7$ corresponds to a grid spacing of $h_r \approx 10^{-7}$, which is a very fine grid. Thus, the un-iterated CHAMP scheme would be stable for

most problems considered in practice.

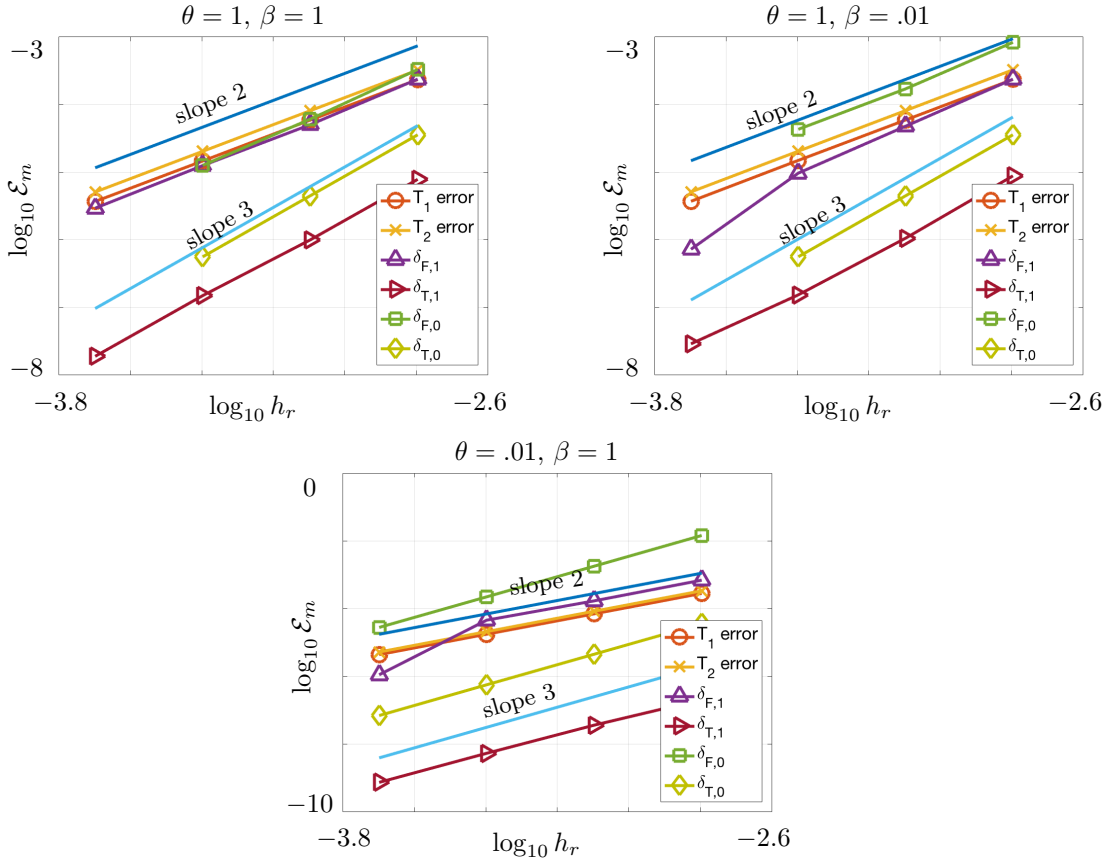

Figure 11: Quarter annulus-annulus: Max-norm errors of temperature along with the jump in heat flux $\delta_{F,k}$, and temperature, $\delta_{T,k}$, at the interface for the Champ scheme with one-iteration at $t_{\text{final}} = 40$ as the grid is refined: Top left: $\theta = 1$ and $\beta = 1$. Top right: $\theta = 1$ and $\beta = 0.01$. Bottom: $\theta = 0.01$ and $\beta = 1$. These plots correspond to the data in Tables 5–7.

For the next test, the thermal diffusivities and conductivities are chosen as $\mathcal{D}_1 = 1$, $\mathcal{D}_2 = 100$ and $\mathcal{K}_1 = \mathcal{K}_2 = 1$, which gives $\theta = 1$ and $\beta = 10^{-2}$. Forcing functions are specified so that $T_e(x, y, t)$ in (101) is the exact solution, and a grid convergence study is performed as before. Results are reported in Table 6. As before we observe second-order accuracy for the un-iterated CHAMP scheme and the scheme with one sub-time-step iteration, and we note that the un-iterated scheme becomes unstable at the finest grid level in agreement with the theoretical stability limit.

For the last test, the thermal properties are chosen as $\mathcal{D}_1 = \mathcal{D}_2 = 1$, $\mathcal{K}_1 = 1$ and $\mathcal{K}_2 = 100$ so that $\theta = 10^{-2}$ and $\beta = 1$, and the convergence results are reported in Table 7. Here, we note second-order accuracy for both versions of the CHAMP time-stepping scheme, and the un-iterated scheme is stable for all grid resolutions. The theory indicates that with θ substantially different from one, as is the case here, the un-iterated scheme is stable for larger values of the parameter $\check{\lambda}_d$. Thus, the results given in the table are in agreement with the theory.

The convergence graphs in Fig. 11 illustrate the behavior of the errors as a function of h_r in log-log plots. Since, when the scheme is stable, the errors in the un-iterated and one-iteration schemes are almost identical, only results for the one-iteration scheme are presented. Note that some data is missing on the finest grid since the scheme was unstable. As expected from values presented in the corresponding tables, the errors are seen to converge at close to second-order.

To investigate the numerical accuracy of the interface jump conditions, equations (3), and (4), we also

plot, in Fig. 11, the residuals in these equations, $\delta_{T,k}$ and $\delta_{F,k}$, defined by

$$\delta_{T,k} = \max_{\mathbf{x}\in\mathcal{I}} \left| \left[T\right]_{\mathcal{I}} \right|, \qquad \delta_{F,k} = \max_{\mathbf{x}\in\mathcal{I}} \left| \left[\mathcal{K}\mathbf{n}\cdot\nabla T\right]_{\mathcal{I}} \right|,$$

where $k = 0$ denotes results from the un-iterated scheme, and $k = 1$ denotes results using one sub-iteration per time-step. In accordance with the theory of Appendix A, the jump in temperature at the interface, $\delta_{T,k}$, is seen to converge at close to third-order accuracy. The jump in the heat-flux, $\delta_{F,k}$, which is a measure of the accuracy of the energy transfer between the domains is seen to converge at close to second-order, again consistent with the theory.

To investigate how the results are affected by taking unoptimized values for the coefficients p_m, the optimized coefficients were scaled by a factor of 1.1, and the examples in this section were recomputed. Results are reported in Table 8 for the most challenging (in terms of stability) of the three test cases when $\mathcal{D}_1 = 1$, $\mathcal{D}_2 = 100$ and $\mathcal{K}_1 = \mathcal{K}_2 = 1$. As before, we observe second-order accuracy for the CHAMP

Quarter annulus-annulus: $\theta = \frac{\mathcal{K}_1}{\mathcal{K}_2} = 1$ and $\beta = \frac{\mathcal{D}_1}{\mathcal{D}_2} = 10^{-2}$										
h_r	Δt	$\tilde{\lambda}_d = \frac{\mathcal{D}_1 \Delta t}{h_r^2}$	un-iterated CHAMP				CHAMP with 1 iteration			
			Domain Ω_1		Domain Ω_2		Domain Ω_1		Domain Ω_2	
			$\mathcal{E}_1$	ratio	$\mathcal{E}_2$	ratio	$\mathcal{E}_1$	ratio	$\mathcal{E}_2$	ratio
1.6e-3	0.8	1.25e+6	2.63e-4	–	3.24e-4	–	2.36e-4	–	3.27e-4	–
8.0e-4	0.4	2.5e+6	unstable	–	unstable	–	5.91e-5	4.00	8.15e-5	4.01
4.0e-4	0.2	5.0e+6	unstable	–	unstable	–	1.49e-5	3.97	2.04e-5	4.00
2.0e-4	0.1	1.0e+7	unstable	–	unstable	–	3.69e-6	4.04	5.09e-6	4.01
rate			–		–		2.0		2.0	

Table 8: Non-optimal weights for the Quarter annulus-annulus with $\theta = 1$ and $\beta = 10^{-2}$: Maximum errors and estimated convergence rates for the un-iterated CHAMP time-stepping scheme and the CHAMP scheme with one sub-time-step iteration. The inner quarter-annulus is the domain Ω_1, while the outer quarter-annulus is Ω_2. These results are computed using non-optimal weights (obtained by artificially scaling the optimized weights by a factor of 1.1) in the CHAMP interface conditions. Compare these results to those in Table 6.

scheme with one sub-time-step iteration for all the mesh spacings considered. Also, the errors in these tests are essentially the same as the previous ones. We note that the un-iterated scheme with non-optimal weights becomes unstable at two additional mesh spacings compared to the case when using the optimized coefficients. This is, however, quite a severe test of the un-iterated scheme, since the time steps Δt chosen in Table 8 are very large, corresponding to very large values of the parameter $\tilde{\lambda}_d$. For example, $\tilde{\lambda}_d = 1.25 \times 10^6$ for the coarse grid case that did still converge. If we instead were to choose $\Delta t \approx h_r$, as is more usual in practice, then the stability limit $\tilde{\lambda}_d \approx 10^6$ would correspond to a grid spacing of $h_r \approx 10^{-6}$, which is a very fine grid.

For the test with $\mathcal{D}_1 = \mathcal{D}_2 = 1$, $\mathcal{K}_1 = 1$ and $\mathcal{K}_2 = 1$, it is also observed (although no table is given) that the un-iterated scheme with non-optimal weights becomes unstable at two additional mesh spacings, while the CHAMP scheme with one sub-time-step iteration is stable in all cases. For the last test with $\mathcal{D}_1 = \mathcal{D}_2 = 1$, $\mathcal{K}_1 = 1$ and $\mathcal{K}_2 = 100$, both the un-iterated and one-iteration CHAMP schemes remain stable for all the test cases; this last test is easier, in accordance with the theory, since θ is substantially different from one. Note that when the scheme is stable it is observed that the errors with non-optimal weights are nearly the same as the errors computed with the optimized parameters.

6.3.2. Two-disks-in-a-square geometry

To verify second-order accuracy of the CHAMP time-stepping scheme for a problem using a more general overlapping grid, we consider the geometry shown in Figure 1 consisting of two disks embedded in a square. For this geometry, domain Ω_1 represents the square with the two disks removed, Ω_2 is the disk at the bottom left, and Ω_3 is the disk at the top right. Domain Ω_1 is bounded by the square $[0, 2] \times [0, 2]$ and is covered by a Cartesian grid with two overlapping annular grids that represent the two circular cut-outs regions (see the right plot in Figure 1). The disk Ω_2 is centered at $(x, y) = (0.65, 0.65)$ and has a radius equal to 0.35.

Two disks in a square: $\frac{\mathcal{K}_1}{\mathcal{K}_2}=10$, $\frac{\mathcal{D}_1}{\mathcal{D}_2}=1$, $\frac{\mathcal{K}_1}{\mathcal{K}_3}=1$, $\frac{\mathcal{D}_1}{\mathcal{D}_3}=10$.							
$h_s^{(j)}$	$\Delta t^{(j)}$	Domain Ω_1		Domain Ω_2		Domain Ω_3	
		$\mathcal{E}_1^{(j)}$	ratio	$\mathcal{E}_2^{(j)}$	ratio	$\mathcal{E}_3^{(j)}$	ratio
1/40	1/40	6.89e-3	–	6.00e-3	–	6.55e-3	–
1/80	1/80	8.02e-4	8.59	1.21e-3	4.96	1.47e-3	4.45
1/160	1/160	2.97e-4	2.70	3.83e-4	3.16	5.17e-4	2.84
1/320	1/320	9.40e-5	3.16	8.79e-5	4.36	1.34e-4	3.86
1/640	1/640	2.36e-5	3.98	1.71e-5	5.13	3.04e-5	4.41
rate		1.95		2.07		1.89	

Table 9: Two disks in a square: Maximum errors and estimated convergence rates at $t_{\text{final}}=1$ for the problem configuration shown in Figure 1. Domain Ω_2 is the lower left disk, Ω_3 the upper right disk, and Ω_1 is the square with the two disks removed.

This domain is covered by a composite grid consisting of a Cartesian grid covering the central portion of the disk and an overlapping interface-fitted annular grid near the interface with the domain Ω_1. The disk Ω_3 is centered at $(x,y)=(1.35,1.35)$ and has a radius equal to 0.35. This domain has a similar composite grid configuration to that of Ω_2. All annular grids have a fixed radial width equal to 0.04375. Let $\mathcal{G}_{\text{tds}}^{(j)}$ denote the multi-domain composite grid, with resolution index j, consisting of all the component grids for all domains. The number of grid points in each coordinate direction for a grid with resolution index j is chosen so that the grid spacing is approximately $h_s^{(j)}=1/(40j)$. The grid shown in Figure 1 is a coarse version of the grid used in the calculations of this section, and the annular grids in the figure have a wider radial width for illustrative purposes.

Forcing functions are applied so that the exact manufactured solution is $T_e(x,y,t)$ given in (101). The initial conditions and the Dirichlet boundary conditions on the perimeter of the square are evaluated from the exact solution. The material coefficients for the three domains are taken as

$$\mathcal{D}_1=10,\quad \mathcal{K}_1=1,\qquad \mathcal{D}_2=10,\quad \mathcal{K}_2=0.1,\qquad \mathcal{D}_3=1,\quad \mathcal{K}_3=1.$$

In this problem there are two different material interfaces, one for each disk. The weighting coefficients p_m in the CHAMP conditions are chosen for each interface independently based on the optimization procedure for the CHAMP time-stepping algorithm described in Section 4.1 and extended to curvilinear grids in Section 5.2.

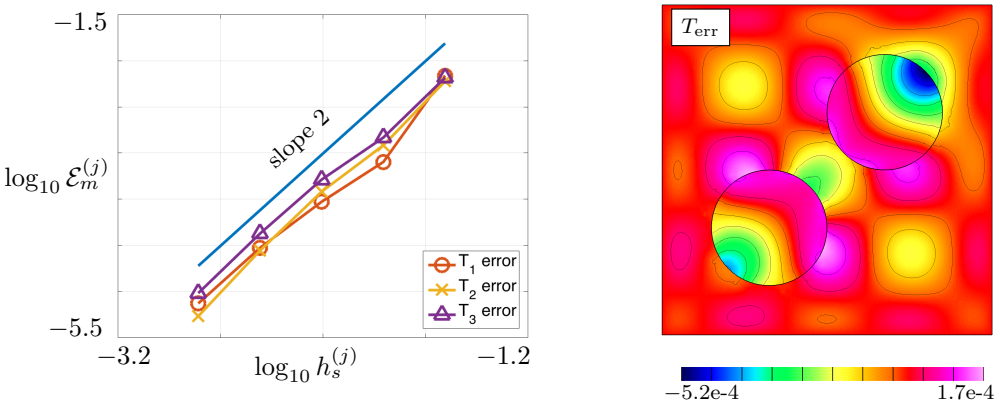

Figure 12: Two disks in a square: Left: max-norm errors in the temperatures $\mathcal{E}_m^{(j)}$ on domain Ω_m at $t_{\text{final}}=1$ for a grid with mesh spacing $h_s^{(j)}$ as the grid is refined. The reference line with slope equal to two indicates second-order accuracy. Right: contours of the error in the temperature at $t_{\text{final}}=1$ for the composite grid $\mathcal{G}_{\text{tds}}^{(3)}$.

Solutions are computed to $t_{\text{final}}=1$, and a convergence study is carried out for a sequence of grids with

increasing resolution given by $\mathcal{G}^{(j)}_{\rm tds}$, $j = 1, 2, 4, 8, 16$. The maximum errors, $\mathcal{E}^{(j)}_m$, for domain Ω_m with grid resolution index j are listed in Table 9. The ratio of successive errors and least-squares estimated convergence rates for each domain are reported as well and indicate second-order accuracy in both space and time. The left plot of Figure 12 illustrates the behavior of the errors as a function of $h^{(j)}_s$ in a log-log plot, and the slope of the curves agree with the reference line for second-order accuracy. The contour plot of the error in the temperature at $t_{\rm final}$ calculated using grid $\mathcal{G}^{(4)}_{\rm tds}$ is shown in the right plot of Figure 12. The error is seen to be smooth in each of the three subdomains, which is a good indication that the solution is well represented on the composite grid. At the interface between subdomains, the error in temperature is small, but not zero as it would be for a scheme with the traditional DN coupling, for example. For the CHAMP scheme, the results here confirm that temperature continuity at the interface is satisfied at the level of the truncation error.

6.4. Self-convergence study for a hexagonal fuel assembly with heat sources

As a final example we consider the solution to a conjugate heat transfer problem that arises when a fluid coolant flows pass an array of hot fuel pins in an hexagonal shaped fuel assembly. This problem is based on the three-dimensional problem considered in Henshaw and Chand [3], but simplified here to two space dimensions and by solving for the temperature alone in the fluid region. The computational domain and a coarse version of the composite grid are plotted in Figure 13. The problem is divided into three different domains which we now describe in turn. Domain Ω_1 consists of the seven cylindrical fuel pins, each of radius 0.5. The fuel pins are located so that the minimum separation distance between the pins and the duct is 0.3. The composite grid for the region interior to each fuel pin is defined using an annular interface-fitted grid together with an inner Cartesian grid (as was done for the disks in Section 6.3.2). The outer solid hexagonal-shaped duct defines domain Ω_2. Its computational domain is defined by an extruded *smooth-polygon* curve with a fixed normal distance of 0.15. The smooth-polygon is defined in terms of logarithms of hyperbolic cosine functions, see [33] for details. Domain Ω_3 is the fluid channel that occupies the region between the fuel pins and the outer duct. The grids for this domain consists of annular grids next to each fuel pin, a smooth-polygon grid next to the solid duct and a background Cartesian grid. Let $\mathcal{G}^{(j)}_{\rm ha}$ denote the multi-domain composite grid for this geometry, where j is the resolution index. The grid spacings for the component grids of $\mathcal{G}^{(j)}_{\rm ha}$ are chosen to be approximately $h^{(j)}_s = 1/(80j)$.

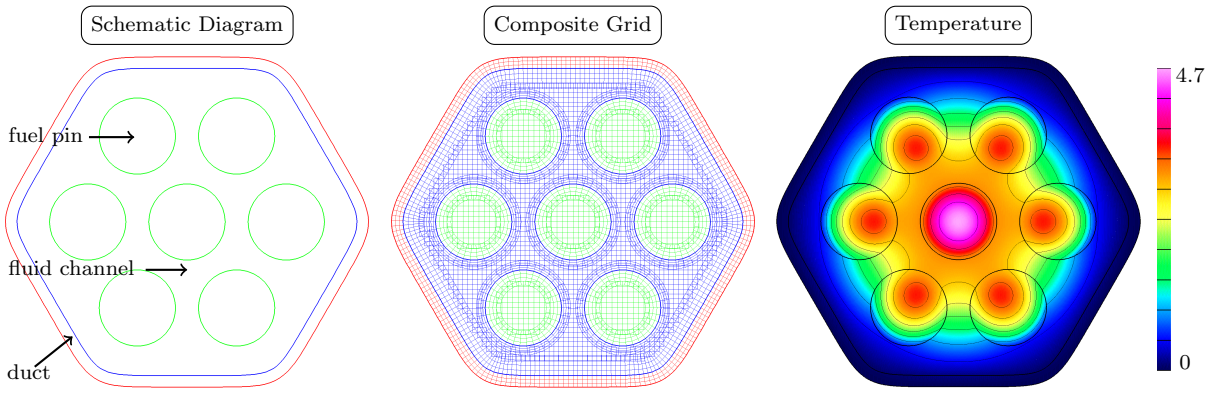

Figure 13: Hexagonal fuel assembly. Left: schematic showing the three sub-domains: solid pins, fluid channel and duct. Middle: a coarse version of the composite grid. Right: computed temperature at $t = 10$ that results from heat sources placed at the center of each pin.

The initial conditions for the temperature in all domains is taken as $T = 0$. The outer hexagonal-shaped boundary of the region is taken as an iso-thermal wall with $T = 0$. A volume heat source, $f(\mathbf{x}, t)$ in (1), is used to heat the region within the fuel pins. The heat source in pin number i is zero at the $t = 0$ and has a smooth representation in space given by

$$f_i(\mathbf{x}, t) = \frac{1}{2}\Big[1 + \text{erf}\Big(12\big(t - \frac{1}{2}\big)\Big)\Big]\Big(\tanh\big(40(r_i + 0.38)\big) + \tanh\big(-40(r_i - 0.38)\big)\Big),$$

where $r_i = |\mathbf{x} - \mathbf{c}_i|$ is the distance of the point $\mathbf{x} = (x, y)$ from the center of the fuel pin at $\mathbf{c}_i$. The total forcing $f(\mathbf{x}, t)$ is set to the sum of the seven individual forcing functions, $f_i(\mathbf{x}, t)$, $i = 1, \ldots, 7$. The parameters for the problem, taken from [3], are

$$\mathcal{D}_1 = 0.1, \quad \mathcal{K}_1 = 0.5, \qquad \mathcal{D}_2 = 0.1, \quad \mathcal{K}_2 = 1, \qquad \mathcal{D}_3 = 0.0694, \quad \mathcal{K}_3 = 0.05,$$

and the equations are integrated to a final time $t_{\text{final}} = 10$.

Hexagonal fuel assembly					
$h_s^{(j)}$	$\Delta t^{(j)}$	$\mathcal{E}_2^{(j)}$	ratio	$\mathcal{E}_\infty^{(j)}$	ratio
1/80	1/10	6.5e-4	–	1.7e-3	–
1/160	1/20	1.5e-4	4.4	3.9e-4	4.4
1/320	1/40	3.3e-5	4.4	8.7e-5	4.5
rate		2.15		2.15	

Table 10: Hexagonal fuel assembly: Estimated errors and convergence rates from a self-convergence study. The discrete L_2 and maximum-norm errors for a grid with resolution index j are denoted by $\mathcal{E}_2^{(j)}$ and $\mathcal{E}_\infty^{(j)}$, respectively.

Numerical solutions are computed for three different grid resolutions using the composite grid $\mathcal{G}_{\text{ha}}^{(j)}$, $j = 1, 2, 4$. The numerical solution for the temperature on the finest grid $\mathcal{G}_{\text{ha}}^{(4)}$ is plotted of the right of Figure 13. Due to the heat sources in each fuel pin, a higher temperature is reached at the center of each pin. Due to the effect of the iso-thermal wall on the perimeter of the duct, heat is leaving the domain through the outer wall and the highest temperature is observed in the central fuel pin. The temperature in the fluid coolant domain is seen to be higher in the interior region located between the ring of six fuel pins and the central pin. Table 10 gives the results of a self-convergence study for this problem. Even though the exact solution is not available for this problem, discrete L_2-norm[11] and maximum-norm errors of the numerical solution for each grid resolution can be estimated using Richardson extrapolation using the procedure described in [34]. These estimated errors are listed in Table 10. The estimated convergence rate is close to two, which again indicates that the CHAMP method is second-order accurate in space and time.

7. Conclusions

We have described a new partitioned algorithm for solving conjugate heat transfer (CHT) problems. The solutions in different material domains are time-stepped in an implicit fashion but coupled at interfaces in an explicit way. This new CHAMP scheme uses generalized Robin (mixed) interface conditions together with a backward differentiation formula in time for the governing PDEs. The new interface treatment combines the usual interface jump conditions for the temperature and heat flux with additional compatibility conditions derived from the governing PDEs; thus extending the optimized-Schwarz method for domain decomposition problems to general CHT problems with material properties that jump at interfaces.

The CHAMP interface conditions can be used as part of an iteration at each time-step as a means to the solve the coupled problem to some error tolerance. A model problem analysis using normal-mode theory was used to understand the convergence properties of the CHAMP iteration and to define an optimization problem that can be solved to determine the optimal weights on the Dirichlet and Neumann-like components in the CHAMP scheme. It was shown that parameters always exist so that the CHAMP iteration will converge for any material properties, grid spacings or time-steps. For domain decomposition problems (i.e. equal material properties) the CHAMP iteration was shown to be better than a typical optimized Schwarz method with overlap width h. When material properties differ, the CHAMP scheme clearly outperforms the classical Dirichlet-Neumann scheme.

[11] The discrete L_2-norm of a grid function $T_{\mathbf{i}}$ is defined by $\|T_{\mathbf{i}}\|_2 = \left\{\sum_{\mathbf{i}} |T_{\mathbf{i}}|^2/N\right\}^{1/2}$, where the sum is taken over all valid grid points on the composite grid and N is the total number of entries in the sum.

The CHAMP interface conditions were incorporated into a partitioned time-stepping algorithm where a fixed number of iterations (perhaps zero iterations) are used at each time-step. In this case the initial guess used in the iteration is important as it affects the accuracy and stability of the scheme; an initial guess based on a third-order accurate extrapolation in time was found to be appropriate for second-order accuracy, in agreement with an error analysis of the scheme. Normal-mode theory was used to analyze the un-iterated CHAMP time-stepping scheme (i.e. one implicit-solve per domain per time-step) and an optimization problem was defined to determine the optimal weights. It was shown that the un-iterated scheme is accurate and stable for a wide range of material properties, grid spacings and time-steps. Including one-additional iteration per time-step greatly enhances the range of stability to likely encompass most practical problems currently of interest.

The CHAMP interface conditions, originally developed for a rectangular geometry, were extended to the case of curvilinear grids. These conditions were implemented in a simulation code for treating general multi-domain problems in two dimensions using composite overlapping grids[12]. A number of test cases were carried out that demonstrated the stability and second-order accuracy of the CHAMP scheme. In addition, the simulations confirmed the results of the model problem analysis and showed that the theory carried over to more complex geometries.

There are a variety of future directions for this work. For example, to address more complex physical situations, the CHAMP scheme could be incorporated into a code for solving true conjugate heat transfer problems involving incompressible flow and heated solids. From the perspective of algorithm development, the CHAMP scheme could be extended to higher-order accuracy and to the cases when the grids on either side of the interface do not match. In addition, one might consider the derivation and implementation of a CHAMP scheme for CHT using other discretization techniques, for example finite elements. Finally, one might consider moving beyond the Gauss-Seidel-like procedure discussed here, for example using an additive Schwarz type method, which may have advantages in terms of algorithmic parallelization.

Appendix A. Accuracy of un-iterated CHAMP time-stepping scheme

In this section we discuss the accuracy of the un-iterated CHAMP time-stepping scheme. The aim is to show that the scheme is second-order accurate. To achieve this, the analysis verifies that the initial guess at each time-step must use third-order accurate extrapolation in time in equation (67). The analysis also shows why the Taylor expansion leading to the CHAMP Neumann operator, $\mathbf{N}_{\theta,\beta,h}$, is truncated at $\mathcal{O}(h^2)$ in equation (48), and why the CHAMP Dirichlet operator, $\mathbf{D}_{\theta,\beta,h}$, is truncated at $\mathcal{O}(h^3)$ in equation (44). For simplicity and clarity we consider a one-dimensional conjugate heat transfer (CHT) problem; a two-dimensional half-plane problem is also straightforward to treat but with additional complexity that serves no great purpose here. We start by deriving an L_2-norm energy estimate for the CHT problem that shows the well-posedness of the problem and provides an estimate for the norm of the solution in terms of norms of the forcings and initial data. This estimate is subsequently used to derive a bound on the error in the *modified equation* for the discrete scheme that shows the second-order accuracy of the approximation.

The one-dimensional CHT problem under consideration is

$$\partial_t T_m - \frac{1}{\rho_m C_m}\partial_x\big(\mathcal{K}_m\partial_x T_m\big) = f_m(x,t), \qquad \text{for } x\in\Omega_m,\ t>0, \tag{A.1a}$$

$$T_L(0,t) - T_R(0,t) = 0, \qquad \text{for } t>0, \tag{A.1b}$$

$$\mathcal{K}_L\partial_x T_L(0,t) - \mathcal{K}_R\partial_x T_R(0,t) = 0, \qquad \text{for } t>0, \tag{A.1c}$$

$$T_L(-1,t) = 0, \quad T_R(1,t) = 0, \qquad \text{for } t>0, \tag{A.1d}$$

$$T_m(x,0) = T_m^{\mathrm{IC}}(x), \qquad \text{for } x\in\Omega_m, \tag{A.1e}$$

for $m = L, R$, where $\Omega_L = [a_L, b_L] = [-1, 0]$ and $\Omega_R = [a_R, b_R] = [0, 1]$, while ρ_m, C_m, and $\mathcal{K}_m$ are assumed to be positive constants. Here we assume that $f_m(x,t)$ and $T_m^{\mathrm{IC}}(x)$ are smooth functions of x and t in which

[12] Using the Overture framework, `overtureFramework.org`.

case $T_m(x,t)$ is also smooth. To derive an L_2-energy estimate, we begin by taking the inner product of $\rho_m C_m T_m$ with (A.1a) over the domain Ω_m which gives

$$\big(\rho_m C_m T_m \,,\, \partial_t T_m\big)_m - \big(T_m \,,\, \partial_x(\mathcal{K}_m \partial_x T_m)\big)_m = \big(\rho_m C_m T_m \,,\, f_m\big)_m,$$

where $(\cdot,\cdot)_m$ denotes the L_2 inner product over Ω_m. Integration by parts on the second term and rearranging gives

$$\frac{1}{2}\frac{d}{dt}\|\sqrt{\rho_m C_m}\, T_m\|_m^2 + \|\sqrt{\mathcal{K}_m}\,\partial_x T_m\|_m^2 - \Big[T_m \mathcal{K}_m \partial_x T_m\Big]_{a_m}^{b_m} = \big(\rho_m C_m T_m \,,\, f_m\big)_m, \tag{A.2}$$

where $\|\cdot\|_m$ is the L_2-norm over Ω_m. Let $T = T(x,t)$ denote the piecewise smooth temperature on the entire domain, being equal to $T_L(x,t)$ on Ω_L and $T_R(x,t)$ on Ω_R. Similarly define ρC, $\mathcal{K}$, $f(x,t)$ and $T^{\mathrm{IC}}(x)$ on the entire domain. Adding the estimates in (A.2) for the left and right domains and using the homogeneous boundary conditions at $x=-1$ and $x=1$ gives

$$\frac{1}{2}\frac{d}{dt}\|\sqrt{\rho C}\, T\|^2 + \|\sqrt{\mathcal{K}}\,\partial_x T\|^2 \;+ \Big(T_R \mathcal{K}_R \partial_x T_R - T_L \mathcal{K}_L \partial_x T_L\Big)\Big|_{x=0} = \big(\rho C T \,,\, f\big), \tag{A.3}$$

where $(\cdot,\cdot)$ and $\|\cdot\|$ denote the L_2 inner product and norm over the entire domain, $x \in [-1,1]$. The difference of interface terms in (A.3) vanishes due to (A.1b) and (A.1c). Furthermore, since the second term on the left-hand side of (A.3) is positive it follows that

$$\|\sqrt{\rho C}\, T\|\;\frac{d}{dt}\|\sqrt{\rho C}\, T\| \;= \frac{1}{2}\frac{d}{dt}\|\sqrt{\rho C}\, T\|^2 \le \big(\rho C T \,,\, f\big) \le \|\sqrt{\rho C}\, T\|\,\|\sqrt{\rho C}\, f\|, \tag{A.4}$$

where we have made use of the Cauchy-Schwarz inequality. Assuming $\|\sqrt{\rho C}\, T\| \neq 0$ we can divide both sides of (A.4) by this quantity to give

$$\frac{d}{dt}\|\sqrt{\rho C} T\| \le \|\sqrt{\rho C}\, f\|. \tag{A.5}$$

Integrating (A.5) in time from 0 to t gives the required energy estimate.

Lemma 2. *The solution to the CHT problem* (A.1a)–(A.1e) *satsifies*

$$\|\sqrt{\rho C}\, T(\cdot,t)\| \le \|\sqrt{\rho C}\, T^{\mathrm{IC}}\| + \int_0^t \|\sqrt{\rho C}\, f(\cdot,\xi)\|\, d\xi. \tag{A.6}$$

The result in (A.6) shows that the weighted L_2-norm of $T(x,t)$ is bounded in terms of norms of the initial conditions and forcing.

We next describe the fully discrete un-iterated CHAMP time-stepping scheme and then derive a *modified-equation* CHT problem corresponding to the scheme. We consider a computational domain in space with grid spacing h, and discretize in time using a time step Δt. Let $x_j = jh$ denote the grid points on either side of the interface with $j \in [-N, -N+1, \ldots, 0] = \Omega_{L,h}$ and $j \in [0, 1, \ldots, N] = \Omega_{R,h}$. The discrete solution is denoted by $\bar{T}^n_{m,j}$, $m = L, R$, which is an approximation of $T_m(x_j, t^n)$. The heat equations and CHAMP interface conditions are discretized in space using standard second-order difference operators [35]

$$D_+\bar{T}^n_{m,j} \stackrel{\text{def}}{=} \frac{\bar{T}^n_{m,j+1} - \bar{T}^n_{m,j}}{h}, \qquad D_-\bar{T}^n_{m,j} \stackrel{\text{def}}{=} \frac{\bar{T}^n_{m,j} - \bar{T}^n_{m,j-1}}{h}, \qquad D_0\bar{T}^n_{m,j} \stackrel{\text{def}}{=} \frac{\bar{T}^n_{m,j+1} - \bar{T}^n_{m,j-1}}{2h}.$$

In order to understand the size of the truncation errors in the CHAMP scheme, an estimate is needed for the size of the coupling parameters $\mathbf{S}_m$, assumed here to be positive, $\mathbf{S}_m > 0$. Note that $\mathbf{S}_m \in \frac{1}{h}[z_m(\kappa = 0), z_m(\kappa = \pi)]$, where z_m is given by (37). Typically, Δt is chosen to be proportional to h for accuracy reasons, and therefore it is expected that $\mathbf{S}_m \in [\mathcal{O}(h^{-\frac{1}{2}}), \mathcal{O}(h^{-1})]$. We thus assume (the somewhat more general condition)

$$\mathbf{S}_m = \mathcal{O}(h^{-p}), \qquad 0 \le p \le 1.$$

The initial guess for the CHAMP interface condition at each step uses extrapolation in time of order q, given by the formulae

$$\mathcal{E}_{-t}^{(q)}(\bar{T}_{R,1}^{n+1}) = \begin{cases} 2\bar{T}_{R,1}^{n} - \bar{T}_{R,1}^{n-1} & \text{for } q = 2, \\ 3\bar{T}_{R,1}^{n} - 3\bar{T}_{R,1}^{n-1} + \bar{T}_{R,1}^{n-2}, & \text{for } q = 3. \end{cases}$$

We consider $q = 2$ or $q = 3$ and show that for second-order accuracy q should be 3 when $\mathbf{S}_m = \mathcal{O}(h^{-p})$, with $0 < p \le 1$. The fully discrete un-iterated CHAMP time-stepping scheme using BDF2 in time is given by

$$\frac{3\bar{T}_{m,j}^{n+1} - 4\bar{T}_{m,j}^{n} + \bar{T}_{m,j}^{n-1}}{2\Delta t} - \mathcal{D}_m D_+ D_- \bar{T}_{m,j}^{n+1} = f_m(x_j, t^{n+1}), \qquad \text{for } j \in \Omega_{m,h},\ n \ge 0, \tag{A.7a}$$

$$\left(\widetilde{\mathbf{N}}_{\theta,\beta,h} + \mathbf{S}_L \widetilde{\mathbf{D}}_{\theta,\beta,h}\right) \bar{T}_{L,0}^{n+1} - (D_0 + \mathbf{S}_L)\left(\mathcal{E}_{-t}^{(q)}(\bar{T}_{R,1}^{n+1})\right) = 0, \qquad \text{for } n \ge 0 \tag{A.7b}$$

$$\left(\widetilde{\mathbf{N}}_{\frac{1}{\theta},\frac{1}{\beta},-h} - \mathbf{S}_R \widetilde{\mathbf{D}}_{\frac{1}{\theta},\frac{1}{\beta},-h}\right) \bar{T}_{R,0}^{n+1} - (D_0 - \mathbf{S}_R)\, \bar{T}_{L,-1}^{n+1} = 0, \qquad \text{for } n \ge 0 \tag{A.7c}$$

$$\bar{T}_{L,-N}^{n+1} = 0, \qquad \bar{T}_{R,N}^{n+1} = 0, \qquad \text{for } n \ge 0 \tag{A.7d}$$

$$\bar{T}_{m,j}^{0} = T_m^{\mathrm{IC}}(x_j), \qquad j \in \tilde{\Omega}_{m,h}, \tag{A.7e}$$

where $\mathcal{D}_m = \mathcal{K}_m/(\rho_m C_m)$, $m = L, R$ are thermal diffusivities and $\tilde{\Omega}_{m,h}$ is an extended grid that includes ghost points, e.g. $\tilde{\Omega}_{L,h} = [-N, -N+1, \ldots, 0, 1]$. The difference approximations of the CHAMP operators, denoted by $\widetilde{\mathbf{D}}_{\theta,\beta,h}$ and $\widetilde{\mathbf{N}}_{\theta,\beta,h}$, are

$$\widetilde{\mathbf{D}}_{\theta,\beta,h} \stackrel{\text{def}}{=} 1 + \theta h D_0 + \frac{h^2}{2}\beta D_+ D_-, \qquad \widetilde{\mathbf{N}}_{\theta,\beta,h} \stackrel{\text{def}}{=} \theta D_0 + h\,\beta D_+ D_-.$$

Past time values needed to start the scheme are assumed to have been determined accurately. We assume that f_m is zero at the interface or else the CHAMP interface conditions would need to be adjusted accordingly. Henceforth we assume that $\Delta t = \mathcal{O}(h)$, which is the usual situation. The scheme also remains second-order accurate if $\Delta t = \mathcal{O}(h^2)$.

We now assume that the discrete approximation (A.7a)–(A.7e) is stable and consistent and thus convergent as $h \to 0$. The formal accuracy of the approximation (A.7a)–(A.7e) can then be accessed from the *modified equation* approach [36] in which a nearby CHT problem is found for a smooth function $\widetilde{T}(x,t)$ which describes well-resolved solutions to the discrete scheme. To leading order, the modified-equation CHT problem corresponding to the discretization in (A.7a)–(A.7e) is

$$\partial_t \widetilde{T}_m - \mathcal{D}_m \partial_x^2 \widetilde{T}_m = f_m(x,t) + \tau^{(2)}, \qquad \text{for } x \in \Omega_m,\ t > 0, \tag{A.8a}$$

$$(\mathbf{N}_{\theta,\beta,h} + \mathbf{S}_L \mathbf{D}_{\theta,\beta,h})\, \widetilde{T}_L(0,t) - (\partial_x + \mathbf{S}_L)\, \widetilde{T}_R(h,t) = \tau^{(2)} + \mathbf{S}_L \tau^{(3,q)}, \qquad \text{for } t > 0, \tag{A.8b}$$

$$\left(\mathbf{N}_{\frac{1}{\theta},\frac{1}{\beta},-h} - \mathbf{S}_R \mathbf{D}_{\frac{1}{\theta},\frac{1}{\beta},-h}\right) \widetilde{T}_R(0,t) - (\partial_x - \mathbf{S}_R)\, \widetilde{T}_L(-h,t) = \tau^{(2)} + \mathbf{S}_R \tau^{(3)}, \qquad \text{for } t > 0, \tag{A.8c}$$

$$\widetilde{T}_L(-1,t) = 0, \quad \widetilde{T}_R(1,t) = 0, \qquad \text{for } t > 0, \tag{A.8d}$$

$$\widetilde{T}_m(x,0) = T_m^{\mathrm{IC}}(x), \qquad \text{for } x \in \Omega_m, \tag{A.8e}$$

where $\mathbf{D}_{\theta,\beta,h}$ and $\mathbf{N}_{\theta,\beta,h}$ are the usual CHAMP operators

$$\mathbf{D}_{\theta,\beta,h} \stackrel{\text{def}}{=} 1 + \theta h \partial_x + \frac{h^2}{2}\beta \partial_x^2, \qquad \mathbf{N}_{\theta,\beta,h} \stackrel{\text{def}}{=} \theta \partial_x + h\,\beta \partial_x^2.$$

The modified equations in (A.8a) and in the CHAMP interface conditions in (A.8b) and (A.8c) include truncation error terms denoted by $\tau^{(2)}$, $\tau^{(3)}$ and $\tau^{(3,q)}$. The precise form of these errors involve various derivatives of $\widetilde{T}_m(x,t)$, but our focus here is on their asymptotic behaviors in the limit $h \to 0$ with $\Delta t = \mathcal{O}(h)$. Accordingly, we introduce the definitions

$$\begin{aligned} \tau^{(2)} &\stackrel{\text{def}}{=} \mathcal{O}(h^2 + \Delta t^2) = \mathcal{O}(h^2), \\ \tau^{(3)} &\stackrel{\text{def}}{=} \mathcal{O}(h^3), \\ \tau^{(3,q)} &\stackrel{\text{def}}{=} \mathcal{O}(h^3 + \Delta t^q) = \mathcal{O}(h^3 + h^q). \end{aligned}$$

It should be noted that terms represented by $\tau^{(2)}$ in different equations may have different functional forms, but the asymptotic behavior for each is $\mathcal{O}(h^2)$. The truncation error terms appearing in (A.8b) and (A.8c) arise from the discrete approximations to the CHAMP Neumann and Dirichlet operators. Note that $\widetilde{\mathbf{N}}_{\theta,\beta,h}$ is an $\mathcal{O}(h^2)$ approximation to $\mathbf{N}_{\theta,\beta,h}$, while due to the extra factors of h that appear in the definition of $\widetilde{\mathbf{D}}_{\theta,\beta,h}$,

$$\begin{aligned}\widetilde{\mathbf{D}}_{\theta,\beta,h}\widetilde{T}_L &= \mathbf{D}_{\theta,\beta,h}\widetilde{T}_L + \theta h\,\frac{h^2}{6}\partial_x^3\widetilde{T}_L(0,t) + \frac{h^2}{2}\beta\,\frac{h^2}{12}\partial_x^4\widetilde{T}_L(0,t) + \mathcal{O}(h^5),\\ &= \mathbf{D}_{\theta,\beta,h}\widetilde{T}_L + \mathcal{O}(h^3),\end{aligned}$$

and thus $\widetilde{\mathbf{D}}_{\theta,\beta,h}$ is a third-order approximation to $\mathbf{D}_{\theta,\beta,h}$ even though D_0 and D_+D_- are only second-order accurate approximations to ∂_x and ∂_x^2, respectively. Here we have used the truncation error formulae

$$D_+D_-T(x_j) = \partial_x^2T(x_j) + \frac{h^2}{12}\partial_x^4T(x_j) + \mathcal{O}(h^4), \qquad D_0T(x_j) = \partial_xT(x_j) + \frac{h^2}{6}\partial_x^3T(x_j) + \mathcal{O}(h^4),$$

which are valid for a sufficiently smooth function $T(x)$.

The CHAMP interface conditions (A.8b)–(A.8c) can be rearranged using Taylor series for $\widetilde{T}_R(h,t)$ and $\widetilde{T}_L(-h,t)$ about $x=0$ along with equation (A.8a) to form[13]

$$\frac{(1+\mathbf{S}_Lh)}{\mathcal{K}_R}\big[\tilde{\sigma}\big]_{\mathcal{I}} + \mathbf{S}_L\big[\widetilde{T}\big]_{\mathcal{I}} + h(1+\mathbf{S}_L\frac{h}{2})\frac{1}{\mathcal{D}_R}\partial_t\big[\widetilde{T}\big]_{\mathcal{I}} = \tau^{(2)} + \mathbf{S}_L\tau^{(3,q)}, \tag{A.9a}$$

$$\frac{(1+\mathbf{S}_Rh)}{\mathcal{K}_L}\big[\tilde{\sigma}\big]_{\mathcal{I}} - \mathbf{S}_R\big[\widetilde{T}\big]_{\mathcal{I}} - h(1+\mathbf{S}_R\frac{h}{2})\frac{1}{\mathcal{D}_L}\partial_t\big[\widetilde{T}\big]_{\mathcal{I}} = \tau^{(2)} + \mathbf{S}_R\tau^{(3)}, \tag{A.9b}$$

where

$$\big[\widetilde{T}\big]_{\mathcal{I}} \stackrel{\text{def}}{=} \widetilde{T}_R(0,t) - \widetilde{T}_L(0,t), \qquad \big[\tilde{\sigma}\big]_{\mathcal{I}} \stackrel{\text{def}}{=} \mathcal{K}_R\widetilde{T}_R(0,t) - \mathcal{K}_L\widetilde{T}_L(0,t),$$

denote the jumps in the temperature and heat flux at the interface, respectively, both functions of time t. Eliminating $\big[\tilde{\sigma}\big]_{\mathcal{I}}$ from (A.9a)–(A.9b) leads to an ODE in time for $\big[\widetilde{T}\big]_{\mathcal{I}}$,

$$(\alpha_L\mathbf{S}_L + \alpha_R\mathbf{S}_R)\big[\widetilde{T}\big]_{\mathcal{I}} + \gamma\,h\,\frac{d}{dt}\big[\widetilde{T}\big]_{\mathcal{I}} = \tau^{(2)} + \alpha_L\mathbf{S}_L\tau^{(3,q)} + \alpha_R\mathbf{S}_R\tau^{(3)}, \tag{A.10}$$

where

$$\alpha_L = \frac{\mathcal{K}_R}{(1+\mathbf{S}_Lh)}, \qquad \alpha_R = \frac{\mathcal{K}_L}{(1+\mathbf{S}_Rh)}, \qquad \gamma = \left(1+\mathbf{S}_L\frac{h}{2}\right)\frac{\alpha_L}{\mathcal{D}_R} + \left(1+\mathbf{S}_R\frac{h}{2}\right)\frac{\alpha_R}{\mathcal{D}_L}.$$

Since $\mathbf{S}_m > 0$ and $\mathbf{S}_m = \mathcal{O}(h^{-p})$, $0 \le p \le 1$, it follows that α_L, α_R and γ are all $\mathcal{O}(1)$. The ODE in (A.10) can be written in the form

$$\frac{d}{dt}\big[\widetilde{T}\big]_{\mathcal{I}} + c\big[\widetilde{T}\big]_{\mathcal{I}} = g(t), \tag{A.11}$$

where

$$c = \frac{(\alpha_L\mathbf{S}_L + \alpha_R\mathbf{S}_R)}{\gamma h} > 0, \qquad g(t) = \frac{\tau^{(2)} + \alpha_L\mathbf{S}_L\tau^{(3,q)} + \alpha_R\mathbf{S}_R\tau^{(3)}}{\gamma h}.$$

The solution of (A.11) is

$$\big[\widetilde{T}\big]_{\mathcal{I}} = [\widetilde{T}]_{\mathcal{I},0}\,e^{-ct} + \int_0^t g(\xi)\,e^{-c(t-\xi)}\,d\xi, \tag{A.12}$$

[13] Recall that we have assumed $f_m(0,t) = 0$. When $f_m(0,t) \neq 0$ the CHAMP interface conditions would need to account for this. The steps leading to (A.9a)–(A.9b) would incorporate these changes but the terms involving $f_m(0,t)$, $m = L, R$, would cancel and thus (A.9a)–(A.9b) would remain unchanged.

where $[\widetilde{T}]_{\mathcal{I},0}$ denotes the value of $\left[\widetilde{T}\right]_{\mathcal{I}}$ at $t=0$. Note that $c=\mathcal{O}(h^{-(1+p)})\gg 1$, so that $\left[\widetilde{T}\right]_{\mathcal{I}}$ decays rapidly onto $g(t)/c$ for small h. This can be seen from (A.12) upon two applications of integration by parts in time:

$$\left[\widetilde{T}\right]_{\mathcal{I}}=\Big([\widetilde{T}]_{\mathcal{I},0}-\frac{1}{c}g(0)+\frac{1}{c^2}g'(0)\Big)e^{-ct}+\frac{1}{c}g(t)-\frac{1}{c^2}g'(t)+\frac{1}{c^2}\int_0^t g''(\xi)e^{-c(t-\xi)}\,d\xi. \tag{A.13}$$

If t is greater than a small time $t_0=1/c=\mathcal{O}(h^{(1+p)})$, i.e. $t\gg t_0$, then the exponential term, e^{-ct}, is small so that (A.13) gives the estimate[14]

$$\left[\widetilde{T}\right]_{\mathcal{I}}=\frac{g(t)}{c}=\frac{1}{(\alpha_L\mathbf{S}_L+\alpha_R\mathbf{S}_R)}\Big(\tau^{(2)}+\alpha_L\mathbf{S}_L\tau^{(3,q)}+\alpha_R\mathbf{S}_R\tau^{(3)}\Big). \tag{A.14}$$

Given (A.14), it then follows from (A.9a) and (A.9b) that the jump in the heat flux at the interface satisfies

$$\left[\tilde{\sigma}\right]_{\mathcal{I}}=\tau^{(2)}+\alpha_L\mathbf{S}_L\tau^{(3,q)}+\alpha_R\mathbf{S}_R\tau^{(3)}. \tag{A.15}$$

Lemma 3. *The jump in the heat flux* $\left[\tilde{\sigma}\right]_{\mathcal{I}}$ *given in* (A.15) *is* $\mathcal{O}(h^2+\Delta t^2)$ *provided*

$$\mathbf{S}_L\,\tau^{(3,q)}=\mathcal{O}(h^2+\Delta t^2).$$

Assuming $\mathbf{S}_L=\mathcal{O}(h^{-p})$, $0\le p\le 1$, *we require*

$$3-p\ge 2\quad \textit{and}\quad q-p\ge 2. \tag{A.16}$$

The first condition in (A.16) *is based on the third-order accurate approximation to the CHAMP Dirichlet operator and thus third order accuracy is required for the case* $0<p\le 1$. *The second condition in* (A.16) *arises from the q-th order time extrapolation, and again if* $0<p\le 1$ *we require* $q=3$ *since the order of extrapolation in time must be a positive integer.*

Furthermore, from (A.14), *the jump in temperature at the interface is expected to be*

$$\left[\widetilde{T}\right]_{\mathcal{I}}=\tau^{(2+p)}\overset{\text{def}}{=}\mathcal{O}(h^{2+p}),\qquad 0\le p\le 1, \tag{A.17}$$

and thus for $p=1$, *i.e.* $\mathbf{S}_m=\mathcal{O}(h^{-1})$, *then this jump would be third-order accurate.*

Under the assumptions that $0\le p\le 1$ and $q=3$, the CHAMP interface conditions in (A.7b) and (A.7c) are equivalent to the original jump conditions on temperature and heat flux perturbed by truncation errors, that is

$$\left[\widetilde{T}\right]_{\mathcal{I}}=\tau^{(2+p)}, \tag{A.18a}$$

$$\left[\tilde{\sigma}\right]_{\mathcal{I}}=\tau^{(2)}. \tag{A.18b}$$

Equations for the errors $E_m=T_m-\widetilde{T}_m$, $m=L,R$, can be formed by subtracting the CHT problem for $\widetilde{T}_m(x,t)$ formed by (A.8a), (A.18a), (A.18b), (A.8d) and (A.8e) from the original CHT problem for $T_m(x,t)$ in (A.1a)–(A.1e). The resulting CHT problem for the error $E_m(x,t)$ has forcing functions proportional to the truncation errors:

$$\partial_t E_m-\mathcal{D}_m\partial_x^2E_m=\tau^{(2)},\qquad \text{for } x\in\Omega_m,\ t>0, \tag{A.19a}$$

$$E_L(0,t)-E_R(0,t)=\tau^{(2+p)},\qquad \text{for } t>0, \tag{A.19b}$$

$$\mathcal{K}_L\partial_xE_R(0,t)-\mathcal{K}_R\partial_xE_L(0,t)=\tau^{(2)},\qquad \text{for } t>0, \tag{A.19c}$$

$$E_L(-1,t)=0,\quad E_R(1,t)=0,\qquad \text{for } t>0, \tag{A.19d}$$

$$E_m(x,0)=0,\qquad \text{for } x\in\Omega_m. \tag{A.19e}$$

[14]Note that this argument shows that even if the jump in the temperature is not small at $t=0$, it will quickly become small after a short time. The fully discrete CHAMP scheme will likely have a similar behavior.

The nonhomogeneous terms on the right-hand sides of the interface conditions in (A.19b) and (A.19c) can be eliminated by constructing a function $W(x,t)$, which is piecewise linear in x and that satisfies the homogeneous boundary conditions at $x=\pm 1$ and the nonhomogeneous interface conditions. This function is $\mathcal{O}(h^2+\Delta t^2)$ owing to the size of the error terms in (A.19b) and (A.19c). Upon subtracting $W(x,t)$ from $E_m(x,t)$, a new error equation for $\tilde{E}_m = E_m - W(x,t)$ results which satisfies the CHT problem

$$\partial_t \tilde{E}_m - \mathcal{D}_m \partial_x^2 \tilde{E}_m = \tau^{(2)}, \qquad \text{for } x \in \Omega_m,\ t>0, \tag{A.20a}$$

$$\tilde{E}_L(0,t) - \tilde{E}_R(0,t) = 0, \qquad \text{for } t>0, \tag{A.20b}$$

$$\mathcal{K}_L \partial_x \tilde{E}_R(0,t) - \mathcal{K}_R \partial_x \tilde{E}_L(0,t) = 0, \qquad \text{for } t>0, \tag{A.20c}$$

$$\tilde{E}_L(-1,t) = 0, \quad \tilde{E}_R(1,t) = 0, \qquad \text{for } t>0 \tag{A.20d}$$

$$\tilde{E}_m(x,0) = \tau^{(2)}, \qquad \text{for } x \in \Omega_m. \tag{A.20e}$$

The energy estimate in (A.6) can now be applied to the CHT problem for the error in (A.20a)–(A.20e) to give

$$\|\sqrt{\rho C}\,\tilde{E}(\cdot,t)\| \le \|\sqrt{\rho C}\,\tilde{E}(\cdot,0)\| + \int_0^t \|\sqrt{\rho C}\,\tau^{(2)}(\cdot,\xi)\|\,d\xi \ = \mathcal{O}(h^2+\Delta t^2). \tag{A.21}$$

We conclude that the CHAMP scheme is second-order accurate when $\mathbf{S}_m = \mathcal{O}(h^{-p})$, $0 \le p \le 1$, provided third-order accurate time-extrapolation is used for (A.7b) when $p>0$. The analysis also indicates why the CHAMP Dirichlet operator is approximated to third-order in h while the Neumann part can be extrapolated to second-order.

References

[1] M. B. Giles, Stability analysis of numerical interface conditions in fluid-structure thermal analysis, Int. J. Numer. Meth. Eng. 25 (1997) 421–436.

[2] B. Roe, R. Jaiman, A. Haselbacher, P. H. Geubelle, Combined interface boundary condition method for coupled thermal simulations, Int. J. Numer. Meth. Fl. 57 (2008) 329–354.

[3] W. D. Henshaw, K. K. Chand, A composite grid solver for conjugate heat transfer in fluid-structure systems, J. Comput. Phys. 228 (2009) 3708–3741.

[4] F.-X. Roux, J.-D. Garaud, Domain decomposition methodology with Robin interface matching conditions for solving strongly coupled fluid-structure problems, International Journal for Multiscale Computational Engineering 7 (1) (2009) 29–38.

[5] A. Heselhaus, A hybrid coupling scheme and stability analysis for coupled solid/fluid turbine blade temperature calculations, in: ASME 1998 International Gas Turbine and Aeroengine Congress and Exhibition, American Society of Mechanical Engineers, 1998, pp. V004T09A014–V004T09A014.

[6] M.-P. Errera, S. Chemin, Optimal solutions of numerical interface conditions in fluid–structure thermal analysis, Journal of Computational Physics 245 (2013) 431–455.

[7] H. A. Schwarz, Ueber einen Grenzübergang durch alternierendes Verfahren, Zürcher u. Furrer, 1870.

[8] M. J. Gander, Optimized Schwarz methods, SIAM J. Numer. Anal. 44 (2) (2006) 699–731.

[9] M. J. Gander, O. Dubois, Optimized Schwarz methods for a diffusion problem with discontinuous coefficient, Numerical Algorithms 69 (2015) 109–144.

[10] Y. T. Peet, P. F. Fischer, Stability analysis of interface temporal discretization in grid overlapping methods, SIAM J. Numer. Anal. 50 (6) (2012) 3375–3401.

[11] R. Jaiman, P. Geubelle, E. Loth, Stable and accurate loosely-coupled scheme for unsteady fluid-structure interaction, paper 2007-334, AIAA (2007).

[12] S. Badia, F. Nobile, C. Vergara, Fluid-structure partitioned procedures based on Robin transmission conditions, J. Comput. Phys. 227 (14) (2008) 7027–7051.

[13] J. W. Banks, B. Sjögreen, A normal mode stability analysis of numerical interface conditions for fluid/structure interaction, Commun. Comput. Phys. 10 (2) (2011) 279–304.

[14] J. W. Banks, W. D. Henshaw, B. Sjögreen, A stable FSI algorithm for light rigid bodies in compressible flow, J. Comput. Phys. 245 (2013) 399–430.

[15] J. W. Banks, W. D. Henshaw, D. W. Schwendeman, An analysis of a new stable partitioned algorithm for FSI problems. Part I: Incompressible flow and elastic solids, J. Comput. Phys. 269 (2014) 108–137.

[16] J. W. Banks, W. D. Henshaw, D. W. Schwendeman, An analysis of a new stable partitioned algorithm for FSI problems. Part II: Incompressible flow and structural shells, J. Comput. Phys. 268 (2014) 399–416.

[17] A. Yenduri, R. Ghoshal, R. Jaiman, A new partitioned staggered scheme for flexible multibody interactions with strong inertial effects, Computer Methods in Applied Mechanics and Engineering 315 (2017) 316 – 347.

[18] G. Chesshire, W. Henshaw, Composite overlapping meshes for the solution of partial differential equations, J. Comput. Phys. 90 (1990) 1–64.

[19] H. S. Carslaw, Introduction to the Mathematical Theory of the Conduction of Heat in Solids, Dover, New York, 1945.

[20] G. Ciaramella, M. J. Gander, Analysis of the parallel Schwarz method for growing chains of fixed-sized subdomains: Part I, SIAM J. Numer. Anal.To appear.

[21] D. R. Jones, C. D. Perttunen, B. E. Stuckman, Lipschitzian optimization without the Lipschitz constant, Journal of Optimization Theory and Applications 79 (1) (1993) 157–181.

[22] M. J. Powell, The BOBYQA algorithm for bound constrained optimization without derivatives, Cambridge NA Report NA2009/06, University of Cambridge, Cambridge.

[23] S. G. Johnson, The NLopt nonlinear-optimization package (2014).

[24] J. C. Strikwerda, Finite Difference Schemes and Partial Differential Equations, Wadsworth and Brooks/Cole, 1989.

[25] J. Verschelde, Algorithm 795: Phcpack: A general-purpose solver for polynomial systems by homotopy continuation, ACM Trans. Math. Softw. 25 (2) (1999) 251–276.

[26] G. F. Carrier, M. Krook, C. E. Pearson, Functions of a Complex Variable: Theory and Technique, Classics in Applied Mathematics, Society for Industrial and Applied Mathematics, Philadelphia, 2005.

[27] J. W. Banks, W. D. Henshaw, D. W. Schwendeman, Deforming composite grids for solving fluid structure problems, J. Comput. Phys. 231 (2012) 3518–3547.

[28] W. D. Henshaw, A high-order accurate parallel solver for Maxwell's equations on overlapping grids, SIAM J. Sci. Comput. 28 (5) (2006) 1730–1765.

[29] P. J. Roache, Code verification by the method of manufactured solutions, ASME J. of Fluids Engineering 124 (1) (2002) 4–10.

[30] D. L. Brown, private communication (1987).

[31] W. D. Henshaw, A fourth-order accurate method for the incompressible Navier-Stokes equations on overlapping grids, J. Comput. Phys. 113 (1) (1994) 13–25.

[32] W. D. Henshaw, G. S. Chesshire, Multigrid on composite meshes, SIAM J. Sci. Comput. 8 (6) (1987) 914–923.

[33] W. D. Henshaw, Mappings for Overture, a description of the Mapping class and documentation for many useful Mappings, Research Report UCRL-MA-132239, Lawrence Livermore National Laboratory (1998).

[34] W. D. Henshaw, D. W. Schwendeman, Parallel computation of three-dimensional flows using overlapping grids with adaptive mesh refinement, J. Comput. Phys. 227 (16) (2008) 7469–7502.

[35] B. Gustafsson, H.-O. Kreiss, J. Oliger, Time Dependent Problems and Difference Methods, John Wiley and Sons Inc., 1995.

[36] R. J. LeVeque, Finite Difference Methods for Ordinary and Partial Differential Equations: Steady-State and Time-Dependent Problems, Society for Industrial and Applied Mathematics, 2007.